Design optimization of structures with path-dependent and non-linear material behavior

Granlund, Gunnar

2025

Document Version:
Publisher's PDF, also known as Version of record

LUND UNIVERSITY

DESIGN OPTIMIZATION OF STRUCTURES WITH PATH-DEPENDENT AND NON-LINEAR MATERIAL BEHAVIOR

GUNNAR GRANLUND

Solid Mechanics

Doctoral Thesis

Design optimization of structures with path-dependent and non-linear material behavior

Gunnar Granlund

LUND
UNIVERSITY

Akademisk avhandling som för avläggande av teknologie doktorsexamen vid tekniska fakulteten vid Lunds universitet kommer att offentligen försvaras torsdagen den 5 juni 2025 klockan 9.00 i sal M:E, M-huset, Ole Römers väg 1, Lund.
Fakultetsopponent: Prof. Kurt Maute, University of Colorado Boulder, USA

Doctoral thesis which by due permission of the Faculty of Engineering at Lund University, will be publicly defended on the 5th of June 2025 at 9.00 a.m. in room M:E of the M-building, Ole Römers väg 1, Lund, Sweden.
Faculty opponent: Prof. Kurt Maute, University of Colorado Boulder, USA

Organization	Document name
LUND UNIVERSITY Division of Solid Mechanics Box 118 SE–221 00 LUND Sweden	**DOCTORAL DISSERTATION** Date of disputation 2025-06-05 Sponsoring organization
Author(s) Gunnar Granlund	

Title and subtitle

Design optimization of structures with path-dependent and non-linear material behavior

Abstract

Topology optimization is a mathematical tool for the computational design of structures, particularly valuable in the early stages of the design process. Gradient-based optimization methods, combined with finite element analysis, form the foundation of an iterative procedure where the design is continuously updated and evaluated. To expand the applicability of topology optimization, this thesis explores a range of design problems involving path-dependent and non-linear material behavior, including hyperelasticity, transient thermo-elasticity, and elasto-plasticity.

The thesis begins with an introduction to topology optimization, followed by formulations, models, and numerical procedures for handling non-linear and path-dependent responses. Thermodynamical principles are presented and linked to constitutive modeling, followed by the balance laws and non-linear solution strategies employed in the optimization frameworks. Topology optimization procedures for both single- and multi-material structures are developed, along with material interpolation schemes tailored to each class of materials. Finally, path-dependent sensitivity analysis is derived and discussed in the context of transient and elasto-plastic problems.

Five appended papers provide detailed studies of specific applications. Paper A introduces a framework for stress-constrained topology optimization of finite strain hyperelastic structures under non-proportional loading, showing that different load trajectories leading to the same terminal state can result in distinct optimal designs. Paper B investigates non-linear transient thermo-elasticity in the design of multi-material thermal actuators, where the material distribution is influenced by the operating time. Papers C–E address the design of 3D elasto-plastic structures for tailored mechanical response, plastic work maximization, self-locking behavior, and stiffness optimization.

Key words

Topology optimization, Path-dependency, Finite strain, Thermo-elasticity, Elasto-plasticity, Path-dependent adjoint sensitivity analysis

Classification system and/or index terms (if any)

Supplementary bibliographical information	Language
	English
ISSN and key title	ISBN
	978-91-8104-437-9 (print) 978-91-8104-438-6 (pdf)
Recipient's notes	Number of pages: 240 / Price
	Security classification

Department of Construction Sciences
Solid Mechanics

ISRN LUTFD2 /TFHF-25/1071-SE(1-240)
ISBN: 978-91-8104-437-9 (print)
ISBN: 978-91-8104-438-6 (pdf)

Design optimization of structures with path-dependent and non-linear material behavior

Doctoral Thesis by

Gunnar Granlund

Printed by Media-Tryck AB, Lund, Sweden
For information, address:
Division of Solid Mechanics, Lund University, Box 118, SE-221 00 Lund, Sweden
Homepage: http://www.solid.lth.se

Yet another small step for mankind...
...one giant leap for the son.

Preface

Writing this thesis, it is impossible not to look back on the past few years and reflect on how I ended up pursuing a PhD. I suppose everyone seeks challenges in different ways, and for me, the pursuit of knowledge and understanding has always been a driving force. In that sense, I am not surprised that engineering, and eventually, solid mechanics, captivated me. The curiosity to understand why materials behave the way they do is what ultimately led me to the Division of Solid Mechanics at Lund University. For that, I am forever grateful.

This journey has involved many people who deserve acknowledgment. First and foremost, I would like to thank my main supervisor, Prof. Mathias Wallin, whose incredible enthusiasm initially drew me to this research field. His guidance and our many conversations, from minor details to major ideas, have been invaluable over the years.

I also want to express my sincere gratitude to Prof. Daniel Tortorelli and Dr. Seth Watts from Lawrence Livermore National Laboratory for thoroughly reviewing and helping me improve my work during the early stages of my PhD. A special thanks goes to Prof. Matti Ristinmaa for always being available for discussions on a variety of topics that have supported the work in this thesis.

Of course, all my colleagues at the division, present and previous, deserve recognition for the enjoyable coffee breaks, the welcoming atmosphere, and fun social times outside of office hours. A special thank you to Dr. Anna Dalklint for all the mentoring and support throughout this period, and to Vilmer Dahlberg for good laughs and PETSc support. I am especially grateful for my office mate, Filip Sjövall, for countless discussions on everything from Lagrange multipliers to track and field.

Thanks also to my friends outside of academia for always encouraging me and simply hanging out. I want to express my deepest gratitude to my family for their unwavering love and support. Last but not least, I thank my beloved wife Johanna for her unconditional love, patience, and support throughout these years. I know the past few months have been tough for you, but you have always been there for me. I will do my very best to be there for both you and our son in the future.

Malmö, April 2025
Gunnar Granlund

Abstract

Topology optimization is a mathematical tool for the computational design of structures, particularly valuable in the early stages of the design process. Gradient-based optimization methods, combined with finite element analysis, form the foundation of an iterative procedure where the design is continuously updated and evaluated. To expand the applicability of topology optimization, this thesis explores a range of design problems involving path-dependent and non-linear material behavior, including hyperelasticity, transient thermo-elasticity, and elasto-plasticity.

The thesis begins with an introduction to topology optimization, followed by formulations, models, and numerical procedures for handling non-linear and path-dependent responses. Thermodynamical principles are presented and linked to constitutive modeling, followed by the balance laws and non-linear solution strategies employed in the optimization frameworks. Topology optimization procedures for both single- and multi-material structures are developed, along with material interpolation schemes tailored to each class of materials. Finally, path-dependent sensitivity analysis is derived and discussed in the context of transient and elasto-plastic problems.

Five appended papers provide detailed studies of specific applications. Paper A introduces a framework for stress-constrained topology optimization of finite strain hyperelastic structures under non-proportional loading, showing that different load trajectories leading to the same terminal state can result in distinct optimal designs. Paper B investigates non-linear transient thermo-elasticity in the design of multi-material thermal actuators, where the material distribution is influenced by the operating time. Papers C–E address the design of 3D elasto-plastic structures for tailored mechanical response, plastic work maximization, self-locking behavior, and stiffness optimization.

Popular Scientific Summary

Computational-driven design is emerging as an efficient approach for creating innovative structures such as engine components, tools, and beams. Central to this approach is Topology Optimization (TO), a proven method for developing efficient and reliable designs. Traditionally, TO has focused on designing extremely stiff, lightweight structures, helping to reduce vehicle mass, optimize material usage, and more. Over time, the method has matured to accommodate additional objectives beyond stiffness and mass, such as constraints on stress, eigenfrequencies, or plastic work.

The process is straightforward: first, the user defines spatial limitations and requirements by specifying a design domain. Then, the constitutive model is chosen, constraints are set, and an objective is selected, e.g., maximizing stiffness. This setup forms the basis of a mathematical optimization problem. Through gradient-based methods, a design is found by evaluating the structural response and incrementally updating the design. This continues until an optimized result is achieved.

To evaluate the physical response of a structure, assumptions about material behavior are necessary. In TO, it is common to assume small deformations with linear elastic behavior due to its simplicity and computational efficiency. However, this thesis aims to push the boundaries of traditional TO by addressing path-dependent and non-linear phenomena.

Path-dependency and non-linearity include various topics, but this thesis specifically covers three key phenomena:

- *Non-proportional loading* refers to complex loading situations where the direction and magnitude of the loads change with time. This thesis introduces a method to design structures capable of withstanding arbitrary load trajectories, accounting for worst-case scenarios that are unknown in both time and space.
- *Transient effects* mean that the material's response changes over time, e.g. thermal heat conduction. This thesis develops a framework for designing thermally driven actuators and demonstrates how the terminal time significantly influences the optimized design.
- *Plastic deformations* are irreversible, which can be utilized to design energy-absorbing or self-locking structures, or harnessed to tailor the mechanical response.

The inclusion of the aforementioned advanced behaviors paves the way for a new class of design challenges and applications, demonstrating that TO can tackle highly complex conditions and push the limits of what is achievable in computational design.

Populärvetenskaplig sammanfattning

Beräkningsdriven design ökar i popularitet som ett effektivt tillvägagångssätt för att hitta nya och hållbara strukturer, såsom motorkomponenter, verktyg eller balkar. Topologioptimering (TO) är en beprövad nyckelmetod för just innovativ design. Historiskt har TO använts för att designa styva och lätta strukturer som med fördel kan användas för att minimera totalvikten på fordon och främja effektiv materialanvändning. Den senaste tiden har metoden tagit ytterligare steg till att omfatta andra beteenden, till exempel villkor på spänningar, egenfrekvenser eller till och med plastiskt arbete.

Processen är ganska enkel: först definierar användaren geometriska begränsningar genom att specificera en designdomän. Därefter väljs en materialmodell, eventuella bivillkor, och ett huvudmål, t.ex. att maximera styvheten. Det visar sig att detta kan formuleras som ett matematiskt optimeringsproblem. Genom gradientbaserade metoder kan man få fram en design genom att kontinuerligt analysera, utvärdera och uppdatera sin design.

För att utvärdera en design krävs att man gör något materialantagande. Inom TO är det vanligt att anta att strukturen genomgår små deformationer med ett linjärelastiskt beteende, vilket är lockande på grund av dess enkelhet och beräkningseffektivitet. I den här avhandlingen är dock målet att vidga området och utforska applikationer som involverar vägberoende och olinjära beteenden.

Vägberoende och olinjäritet kan innebära många saker, men denna avhandling kretsar specifikt kring tre nyckelfenomen:

- *Icke-proportionell belastning* avser komplexa belastningssituationer där lasternas riktning och storlek förändras över tid. Avhandlingen presenterar en metod för att designa strukturer som kan hantera en godtycklig lasthistorik och ta hänsyn till värsta tänkbara scenario trots att det är okänt i både tid och rum.
- *Transienta effekter* innebär att materialets respons förändras över tid, t.ex. vid värmeledning. Avhandlingen utvecklar ett ramverk för att designa termiskt drivna mekanismer och visar hur sluttiden har stor påverkan på den optimerade designen.
- *Plastiska deformationer* är irreversibla och kan utnyttjas för att designa energiabsorberande strukturer, självlåsande mekanismer, eller för att skräddarsy den mekaniska responsen.

Genom att inkludera dessa avancerade beteenden kan en helt ny klass av designutmaningar och tillämpningar utforskas. Detta visar att TO kan hantera mycket komplexa förhållanden och flyttar gränserna för vad som är möjligt inom beräkningsdriven design.

List of appended papers

This doctoral thesis is based on the following manuscripts:

Paper A
Gunnar Granlund, Mathias Wallin, Daniel Tortorelli, and Seth Watts
Stress-constrained topology optimization of structures subjected to nonproportional loading
International Journal for Numerical Methods in Engineering, 124.12 (2023): 2818-2836

Paper B
Gunnar Granlund, Mathias Wallin, Olov Günther-Hanssen, Daniel Tortorelli, and Seth Watts
Topology optimization of compliant mechanisms under transient thermal conditions
Computer Methods in Applied Mechanics and Engineering 418 (2024): 116478

Paper C
Gunnar Granlund and Mathias Wallin
Large-scale elasto-plastic topology optimization
International Journal for Numerical Methods in Engineering, (2024): e7583

Paper D
Gunnar Granlund and Mathias Wallin
Designing compliant self-locking structures using topology optimization
Accepted for publication in Structural and Multidisciplinary Optimization

Paper E
Gunnar Granlund and Mathias Wallin
Design of stiff elasto-plastic structures
To be submitted for publication

Own Contribution
The author of this thesis has taken the main responsibility for the preparation and writing of all appended papers. The numerical models have been developed in collaboration with the co-authors, whereas the implementation of the models has been conducted by the first author.

Contents

Chapter 1

Introduction

Computational-driven design has gained popularity in recent years. The method utilize computational resources and algorithms in the design process when developing structural components and products. This approach not only reduces the time required for design but also ensures that structural integrity is considered throughout the process. One such method is topology optimization, which serves as a mathematical approach to design structures by formulating and solving an optimization problem.

1 Evolution and Applications of Topology Optimization

The early work of Bendsøe and Kikuchi (1988) paved the way for the modern density-based approach commonly referred to as topology optimization. Initially, it was applied to linear elastic structures, optimizing stiffness under a prescribed mass constraint, an objective that remains common today. Another early application was the design of compliant mechanisms (Sigmund (1997), Bruns and Tortorelli (2001)), which are flexible structures that use elastic deformation to transmit motion and forces. A comprehensive review of topology optimization and its applications can be found in Sigmund and Maute (2013).

The goal of topology optimization is to find an optimal solution to a problem defined by performance criteria and certain constraints, such as material usage. Fig. 1.1 illustrates the procedure, where boundary conditions, such as prescribed displacements and loads, are defined on a design domain that sets the geometrical restrictions. An objective is formulated, for example, to maximize the motion in a certain direction (indicated by the vertical arrows in Fig. 1.1), along with constraints, such as material usage, max stresses, or displacement in certain points.

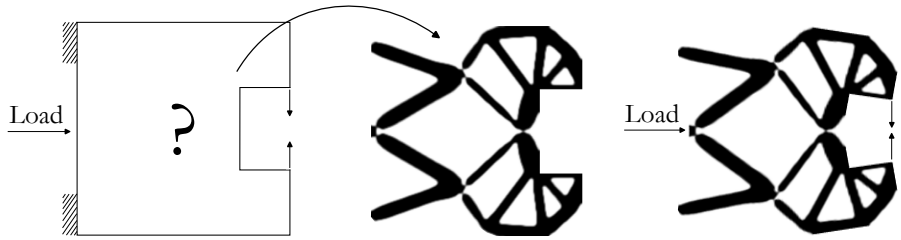

Figure 1.1: Topology optimization procedure of a compliant gripper mechanism.

The field has matured, enabling the study of more complex objectives and constraints. The natural extension from stiffness is stress, which is often incorporated as a constraint (Cheng and Guo (1997), Duysinx and Bendsøe (1998), Le et al. (2010)). From an engineering perspective, eigenfrequencies (Pedersen (2000), Dalklint et al. (2020)) and buckling criteria (Neves et al. (1995), Gao and Ma (2015), Ferrari and Sigmund (2019)) are of high interest.

In addition to mechanical systems, topology optimization has been successfully applied to other physics domains, such as thermal conduction (Gersborg-Hansen et al. (2006), Gao et al. (2008)), enabling the design of structures with optimized heat transfer properties. Dbouk (2017) provides an overview of topology optimization applications for conductive, convective, and conjugate heat transfer. Coupled multiphysics problems have also been explored, with actuators being a particularly popular topic. Notable examples include thermo-mechanical and electro-mechanical mechanisms (Sigmund (2001a), Li et al. (2004)), and actuators modeled with electroactive polymers Hård et al. (2024). The design space can also be expanded by incorporating multiple materials into the framework, allowing different material properties to be efficiently utilized (Sigmund (2001b), Giraldo-Londoño et al. (2020)).

A limitation of most available studies is that they primarily consider 2D problems, as the computational cost of designing 3D structures is significantly higher. However, large-scale problems have gained popularity in recent years, and numerous guidelines on parallel communication, memory distribution (Borrvall and Petersson (2001a), Aage et al. (2015)), iterative solver setups (Amir et al. (2010)), and GPU acceleration (Träff et al. (2023)) are now available, enabling design problems with multi-million-element 3D models (see Fig. 1.2). Aage et al. (2017) demonstrated the potential of topology optimization as a large-scale design tool by presenting giga-voxel topology optimization of a full aircraft wing, discretized using 1.1 billion finite elements.

To formulate the optimization problem, a design representation is required. The most common approach is density-based, where a design field is introduced to describe the material distribution as a density or volume fraction at each point. One early approach

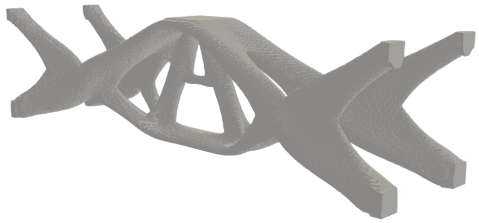

Figure 1.2: Design optimized for plastic work maximization discretized using 65 million finite elements (Granlund and Wallin (2024)).

was the homogenization method (Bendsøe and Kikuchi (1988)), which models material as a porous microstructure, while modern density-based methods typically interpolate material properties directly via the design variables. To enforce nearly discrete designs, interpolation schemes often include penalization of intermediate density regions, such as in the Solid Isotropic Material with Penalization (SIMP) method (Bendsøe (1989)) or the Rational Approximation of Material Properties (RAMP) method (Stolpe and Svanberg (2001)).

Another approach is the level-set method, where an implicit function is used to define the material interface (Sethian (2001), Osher and Fedkiw (2001), Allaire et al. (2004)). Unlike density-based methods, the level-set method provides a sharp boundary representation, which can improve the accuracy of the mechanical response near interfaces. A review of level-set methods for structural topology optimization can be found in Van Dijk et al. (2013).

A third possibility includes the phase-field method (Bourdin and Chambolle (2003), Blank et al. (2012), Wallin et al. (2012)), where a phase-field variable is introduced to represent the material distribution. Instead of sharp material interfaces, the method employs a diffuse interface approach, where the transition between solid and void is governed by a gradient-dependent regularization term. This allows for natural topological changes, such as merging and splitting, while ensuring numerical stability through interface modeling.

The number of applications has rapidly increased over the years, but many areas remain to be explored. Much of the work to date has been restricted to linear elastic material behavior and simple loading cases. To expand the method's applicability for industrial applications, this thesis examines non-linear material descriptions and path-dependent responses, demonstrating that topology optimization can be applied to design problems under highly complex conditions.

2 Path-dependency and Non-linear Materials

Under small strains, most materials can be approximated as linear, and if the load remains low, deformations are often reversible, eliminating the need to track plastic strains. However, non-linear responses, such as finite strains, geometric nonlinearity, or inelastic behavior, are common in engineering applications where the linear elastic assumption breaks down. For these applications, topology optimization frameworks need to account for non-linear phenomena to be useful.

Before fracture or necking occur, the material response can be divided into elastic and plastic parts. Fig. 1.3 shows a schematic graph of a stress-strain response for a linear elastic, non-linear elastic and elasto-plastic material. Reversed arrows symbolize reversed loading, where the elastic response is reversible and returns to the initial state, whereas the plastic response is irreversible, resulting in a permanently deformed state upon unloading.

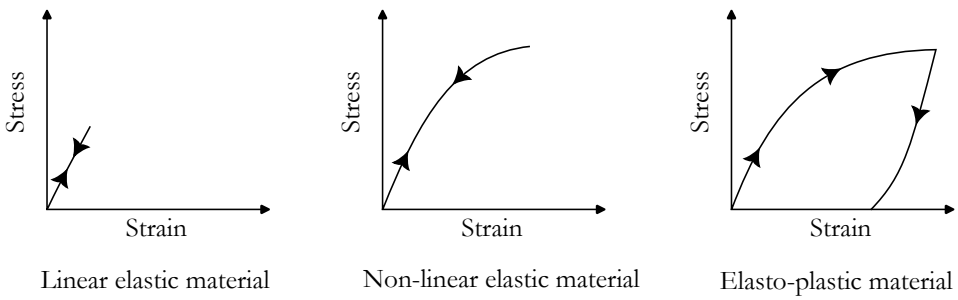

Figure 1.3: Schematic graph of a stress-strain relationship with reversed loading for linear elastic, non-linear elastic and elasto-plastic materials.

As seen in Fig. 1.3, the linear elastic assumption is restricted to a limited range of loading. By extending to non-linear elasticity and kinematics, effects from finite strains and geometrical non-linearities can be captured. Several studies have highlighted the importance of considering large deformations in the topology optimization framework. Geometrical non-linearities are considered by Bruns and Tortorelli (2001) in the design of compliant mechanisms, and they present significant differences in the optimized designs. Similar findings were presented by Kemmler et al. (2005), who explored the impact of different stiffness definitions, which are not unique in the case of large deformations. An extension is provided by Wallin et al. (2018), who considered general finite strain hyperelasticity when designing stiff structures and demonstrated substantial differences in optimized designs depending on the load magnitude.

Elasticity is, by definition, reversible, which simplifies the optimization setup since the load history does not affect the terminal state. In path-dependent problems the state at

each time step depends on the state in the previous step, requiring a temporal discretization. These problems are usually modeled as initial value problems (IVPs), where the initial state is used as a starting point to compute the state evolution using time integration. The starting point and the load history affect the terminal state, introducing a path-dependency. From an optimization perspective, the path-dependency requires that the entire state history must be stored for gradient computations, in contrast to elastic problems, introducing computational challenges.

Transient effects in heat conduction have previously been explored. In the case of minimizing the maximum temperature, Wu et al. (2019) showed that the optimized design has a significant dependency on the terminal time, demonstrating that for practical applications, one should not consider only steady state situations. An extension to transient thermo-mechanical systems in the design of thermal actuators that should operate within a certain time interval is provided in Granlund et al. (2024).

Including plasticity in the framework allows mechanically dissipative structures to be designed. An early work on elasto-plastic topology optimization was conducted by Maute et al. (1998), where structures with maximized structural ductility. Energy absorption is a popular application for elasto-plastic topology optimization (Kato et al. (2015), Wallin et al. (2016), Ivarsson et al. (2018), Russ and Waisman (2021), Abueidda et al. (2021)), commonly formulated as plastic work maximization problems. However, other applications exist, such as mechanical response tailoring (Pedersen (2003), Granlund and Wallin (2024), peak plastic work minimization (Amir (2017), Ivarsson et al. (2021)), or in permanent lock mechanism design (Granlund and Wallin (2025).

3 Research aim

This thesis develops methods for designing structures undergoing transient, path-dependent and non-linear behavior. The path-dependent phenomena covered in this thesis include non-proportional loading, thermal transient effects, and elasto-plasticity. Papers A and B cover hyperelastic and thermo-hyperelastic materials, while papers C-E address small strain elasto-plasticity with both isotropic and kinematic hardening models.

Paper A provides a methodology for designing structures subject to non-proportional loading with stress constraints, where the peak stress is unknown in space and time. Paper B presents a framework for designing thermal actuators that should operate within specific time intervals. In paper C, a framework for large-scale elasto-plastic problems is presented, demonstrating the use of 3D structures discretized with multi-million elements. Papers D and E extend the applications of elasto-plastic topology optimization by introducing two new design problems: self-locking structures and "stiff" elasto-plastic structures.

Chapter 2

Field equations and constitutive models

The governing field equations describe the behavior of a physical system over a domain. These equations stem from fundamental principles such as conservation laws and constitutive relations and typically involve spatial and temporal variables. This chapter presents the fundamental governing equations necessary for the subsequent topology optimization framework. It covers kinematics, balance laws, thermodynamics, and constitutive modeling, with focus on elasto-plasticity and thermo-elasticity. Additionally, derivations are provided to enhance understanding of the constitutive models. Further information on the topics included in this chapter can be found in e.g. Holzapfel (2000), Ottosen and Ristinmaa (2005), and Simo and Hughes (2006).

1 Kinematics

In a finite strain setting, the deformed configuration Ω is distinguished from the reference configuration Ω_o. The motion of a material particle initially located at position $\boldsymbol{X} \in \Omega_o$ is described by a smooth mapping so that the current position is $\boldsymbol{x} = \boldsymbol{\varphi}(\boldsymbol{X}, t) = \boldsymbol{X} + \boldsymbol{u}(\boldsymbol{X}, t)$, $\boldsymbol{\varphi} : \Omega_o \text{ x } I \to \mathbb{R}^3$, where $\boldsymbol{u} : \Omega_o \text{ x } I \to \mathbb{R}^3$ is the displacement and $I = [0, T]$ the time interval. In the case of a coupled thermo-mechanical formulation, $\theta : \Omega_o \text{ x } I \to \mathbb{R}$ is the temperature. The boundary of the body Ω_o is denoted $\partial\Omega_o = \partial\Omega_{oD}^{\mathcal{B}} \cup \partial\Omega_{oN}^{\mathcal{B}}$ with the outward normal unit vector $\boldsymbol{n}_o$. Dirichlet boundary conditions are applied to $\partial\Omega_{oD}^{\mathcal{B}}$ and Neumann boundary conditions to $\partial\Omega_{oN}^{\mathcal{B}}$ [1]. This is illustrated in Fig. 2.1, which depicts the reference configuration Ω_o and the deformed configuration Ω.

[1] To differentiate boundary value problems, $\mathcal{B}$ represents a problem, e.g. mechanical with prescribed displacement $\bar{\boldsymbol{u}}$ and traction $\bar{\boldsymbol{t}}$, or thermal with prescribed temperature θ and heat flux $\bar{q}$.

The deformation in the neighborhood of $\boldsymbol{X}$ is described by the deformation gradient $\boldsymbol{F} = \nabla\boldsymbol{\varphi}$, where ∇ is the material gradient operator on Ω_o. The determinant of $\boldsymbol{F}$, denoted $J = \det(\boldsymbol{F})$, represents local volume changes. To ensure a one-to-one mapping, $\boldsymbol{\varphi}$ must satisfy $J > 0$ at all points in the domain. Local deformations are described by the right Cauchy-Green deformation tensor

$$\boldsymbol{C} = \boldsymbol{F}^{\mathrm{T}}\boldsymbol{F}, \tag{2.1}$$

and the Green-Lagrange strain tensor

$$\boldsymbol{E} = \frac{1}{2}\left(\boldsymbol{C} - \boldsymbol{I}\right), \tag{2.2}$$

where $\boldsymbol{I}$ denotes the second order unit tensor.

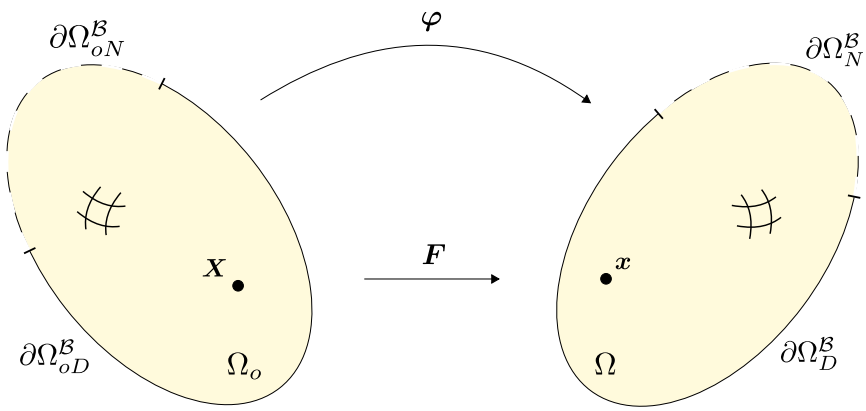

Figure 2.1: Deformation of a body with the reference configuration Ω_o to the left, and the deformed configuration Ω to the right.

In the limit of small strains and rotations, the linearized strain

$$\boldsymbol{\epsilon} = \frac{1}{2}\left(\left(\nabla\boldsymbol{u}\right)^{\mathrm{T}} + \nabla\boldsymbol{u}\right), \tag{2.3}$$

is used to describe local deformations. The reference and deformed configurations coincide in small strain theory.

2 Thermodynamics

Having established measures for deformation and strain, the thermodynamic principles that constrain the form of admissible constitutive laws are now introduced. These constraints ensure physically meaningful material behavior.

The first and second laws of thermodynamics govern energy conservation and irreversibility, respectively. These laws impose fundamental constraints on admissible constitutive models.

The first law of thermodynamics expresses the conservation of energy. In its local form, in the reference configuration, it is given by

$$\rho_o \dot{u} = \boldsymbol{P} : \dot{\boldsymbol{F}} + \rho_o r - \nabla \cdot \boldsymbol{q}_o, \tag{2.4}$$

where u is the internal energy per unit mass, $\boldsymbol{P}$ the first Piola-Kirchhoff stress tensor, r the external heat source per unit mass and $\boldsymbol{q}_o$ the heat flux vector in the reference configuration. As shown in the next section, the first law of thermodynamics (2.4) can be used to provide the generalized heat equation.

The second law of thermodynamics governs the directionality of energy transfer. For physical consistency, constitutive models must satisfy the second law of thermodynamics. The Clausius-Duhem inequality places restrictions on constitutive models, preventing unphysical energy generation, and for continuum mechanics, the local form of the second law stems from the Clausius-Duhem inequality and can be rewritten as the dissipation inequality

$$\mathcal{D} = \rho_o \theta \dot{\eta} - \rho_o \dot{u} + \boldsymbol{P} : \dot{\boldsymbol{F}} - \frac{1}{\theta} \boldsymbol{q}_o \cdot \nabla \theta \geq 0, \tag{2.5}$$

where the specific entropy per unit mass η, and the absolute temperature θ, are introduced. The internal energy depends on certain material quantities $\boldsymbol{A}$ and the entropy η, i.e. $u = u(\boldsymbol{A}, \eta)$. The state variables in $\boldsymbol{A}$ includes $\boldsymbol{F}$, but could also include variables governing e.g. plastic hardening. To express (2.5) in terms of $\boldsymbol{A}$ and θ, a Legendre transformation of the internal energy provides

$$u(\boldsymbol{A}, \eta) = \psi(\boldsymbol{A}, \theta) + \theta \eta, \tag{2.6}$$

where ψ is Helmholtz free energy. Using (2.6) in (2.5), and using the arguments of the Coleman-Noll procedure, it is shown that $\eta = -\frac{\partial \psi}{\partial \theta}$, and (2.5) becomes

$$\mathcal{D} = \underbrace{\boldsymbol{P} : \dot{\boldsymbol{F}} - \rho_o \frac{\partial \psi}{\partial \boldsymbol{A}} : \dot{\boldsymbol{A}}}_{\mathcal{D}_{mech}} \underbrace{- \frac{1}{\theta} \boldsymbol{q}_o \cdot \nabla \theta}_{\mathcal{D}_{therm}} \geq 0. \tag{2.7}$$

The dissipation inequality should hold for any thermodynamic state, and is thus divided into $\mathcal{D} = \mathcal{D}_{mech} + \mathcal{D}_{therm}$, which corresponds to the mechanical and thermal dissipation, respectively.

The thermal dissipation inequality is always satisfied based on physical observations, and the constitutive models should be chosen so that the mechanical dissipation is fulfilled. This will be demonstrated later in this chapter for hyperelasticity, coupled thermo-hyperelasticity, and elasto-plasticity.

3 Balance laws

The balance laws for mass, momentum, and energy must hold for any material. However, their specific forms are influenced by thermodynamic principles, particularly the second law, which ensures physically consistent energy dissipation.

In the absence of body forces and inertia, the balance of linear momentum simplifies to the equilibrium equation

$$\begin{aligned} &\nabla \cdot \boldsymbol{P} = \boldsymbol{0} \text{ in } \Omega_o, \\ &\boldsymbol{P} \cdot \boldsymbol{n}_o = \bar{\boldsymbol{t}} \text{ on } \partial\Omega_{oN}^{\mathcal{M}}, \\ &\boldsymbol{u} = \bar{\boldsymbol{u}} \text{ on } \partial\Omega_{oD}^{\mathcal{M}}, \end{aligned} \tag{2.8}$$

where $\boldsymbol{u}$ the displacement vector, and superscript $\mathcal{M}$ represents the mechanical boundary value problem where prescribed traction $\bar{\boldsymbol{t}}$ and displacements $\bar{\boldsymbol{u}}$ are prescribed on respective portion of the boundary $\partial\Omega_o$.

The coupled heat equation can be derived from the first law of thermodynamics (2.4). Using Helmholtz's free energy (2.6) in (2.4) provides

$$\rho_o \left(\frac{\partial \psi}{\partial \boldsymbol{A}} : \dot{\boldsymbol{A}} + \theta \dot{\eta} \right) = \boldsymbol{P} : \dot{\boldsymbol{F}} + \rho_o r - \nabla \cdot \boldsymbol{q}_o, \tag{2.9}$$

and since $\eta = -\frac{\partial \psi}{\partial \theta}$, (2.9) is extended to

$$\begin{aligned} &\rho_o c \dot{\theta} = \mathcal{D}_{mech} + \rho_o r + \rho_o \theta \frac{\partial^2 \psi}{\partial \theta \partial \boldsymbol{A}} : \dot{\boldsymbol{A}} - \nabla \cdot \boldsymbol{q}_o \text{ in } \Omega_o \\ &\boldsymbol{q}_o \cdot \boldsymbol{n}_o = \bar{q} \text{ on } \partial\Omega_{oN}^{\mathcal{T}}, \\ &\theta = \bar{\theta} \text{ on } \partial\Omega_{oD}^{\mathcal{T}}, \end{aligned} \tag{2.10}$$

where $c = -\theta \frac{\partial^2 \psi}{\partial \theta^2}$ is the specific heat capacity. The mixed term $\rho_o \theta \frac{\partial^2 \psi}{\partial \boldsymbol{A} \partial \theta} : \dot{\boldsymbol{A}}$ gives rise to the so-called the Kelvin-Joule effect and represents thermo-elastic coupling. The superscript $\mathcal{T}$ represents the boundaries of the thermal boundary value problem where heat flux $\bar{q}$ and temperatures $\bar{\theta}$ are prescribed.

4 Constitutive models

While the balance equations describe general conservation principles, they must be supplemented with material specific constitutive laws. In the following, constitutive models for hyperelasticity, coupled thermo-hyperelasticity and elasto-plasticity are introduced, ensuring consistency with thermodynamic principles.

The constitutive models that describe the material behavior under different loading conditions needs to fulfill the dissipation inequality (2.5). This is straight forward for reversible processes, such as elasticity, where the mechanical dissipation is zero. For irreversible elasto-plastic problems however, it will be shown that the plastic flow can not be described by a single potential function ψ.

4.1 Hyperelasticity

A hyperelastic material is modeled using a constitutive law where the stress-strain relationship derives from a strain energy density function. Many hyperelastic models exist and are discussed in e.g. Holzapfel (2000). In Paper A, a compressible neo-Hookean model has been used defined by the strain energy density function

$$\rho_o \psi = \frac{1}{4}\kappa \left(\left(J^2 - 1 \right) - \ln \left(J^2 \right) \right) + \frac{1}{2}\mu \left(J^{-2/3} \mathrm{tr} \left(\boldsymbol{C} \right) - 3 \right), \tag{2.11}$$

where κ and μ, in the limit of infinitesimal strain, correspond to the bulk and shear moduli. The first Piola-Kirchhoff stress that appears in (2.8) is given by the derivative of the strain energy function with respect to the deformation gradient, i.e.

$$\boldsymbol{P} = \rho_o \frac{\partial \psi}{\partial \boldsymbol{F}}. \tag{2.12}$$

The first Piola-Kirchhoff stress, $\boldsymbol{P}$, relates the forces in the current configuration with the areas in the reference configuration. To obtain a stress measurement that relates the forces in the current configuration to the areas in the current configuration, a Piola transformation of $\boldsymbol{P}$ is used to write $\boldsymbol{\sigma} = \frac{1}{J}\boldsymbol{P}\boldsymbol{F}^{\mathrm{T}}$, where $\boldsymbol{\sigma}$ is the Cauchy stress tensor. Likewise, to obtain a stress measure that relates the forces in the reference configuration to the areas in the reference configuration, the second Piola-Kirchhoff stress is obtained from $\boldsymbol{S} = \boldsymbol{F}^{-1}\boldsymbol{P} = 2\rho_o \frac{\partial \psi}{\partial \boldsymbol{C}}$.

For completeness, the incremental elasticity tensor, here expressed in the reference configuration, required to solve the boundary value problem using the total Lagrangian formulation is given by

$$\mathbb{D} = 4\rho_o \frac{\partial^2 \psi}{\partial \boldsymbol{C} \partial \boldsymbol{C}}. \tag{2.13}$$

4.2 Coupled thermo-hyperelasticity

To include thermal effects, the neo-Hookean strain energy density function can be extended to include the temperature θ, where

$$\rho_o \psi = \kappa \left[\tfrac{1}{2} (\ln (J))^2 - 3\alpha_{th} (\theta - \theta_0) \ln (J) \right] + \tfrac{1}{2}\mu \left(J^{-2/3} \mathrm{tr} \left(\boldsymbol{C} \right) - 3 \right) + T(\theta), \tag{2.14}$$

is used in Paper B. In (2.14), α_{th} is the thermal expansion coefficient and is in general temperature-dependent, θ_0 a reference temperature, and the function $T(\theta)$ is related to the specific heat capacity. The heat flux vector follows from Fourier's law and is expressed in the reference configuration as

$$\boldsymbol{q}_o = -J\boldsymbol{F}^{-1}\boldsymbol{\kappa}_c\boldsymbol{F}^{-\mathrm{T}}\nabla\theta, \tag{2.15}$$

where $\boldsymbol{\kappa}_c = \kappa_c\boldsymbol{I}$ is the uniform isotropic spatial conductivity tensor.

Thermomechanical systems for large deformations are commonly based on a multiplicative split of the deformation gradient, i.e.

$$\boldsymbol{F} = \boldsymbol{F}^e\boldsymbol{F}^\theta, \tag{2.16}$$

where $\boldsymbol{F}^e$ describes the elastic contribution and $\boldsymbol{F}^\theta$ the thermal.

Assuming the thermal expansion to be purely isotropic volumetric renders $\boldsymbol{F}^\theta = \left(J^\theta\right)^{1/3}\boldsymbol{I}$, with $J^\theta = e^{3\alpha_{th}(\theta-\theta_0)}$. This shows that the isochoric contribution in (2.14) is based purely on the elastic deformations as

$$J^{-2/3}\mathrm{tr}\left(\boldsymbol{C}\right) = J^{e\,-2/3}\mathrm{tr}\left(\boldsymbol{C}^e\right). \tag{2.17}$$

The multiplicative split can also be considered when determining $T(\theta)$ by studying the case when the temperature increases without inducing any elastic deformations. Since the strain energy should only vary with elastic deformations, considering the case $\boldsymbol{F} = \boldsymbol{F}^\theta$, shows that

$$T(\theta) = \frac{1}{2}\kappa\left(3\alpha_{th}\left(\theta-\theta_0\right)\right)^2, \tag{2.18}$$

for this particular choice of strain energy density function (2.14).

4.3 Small strain elasto-plasticty

For small strain elasto-plasticity, the additive split of the strain tensor

$$\boldsymbol{\epsilon} = \boldsymbol{\epsilon}^{el} + \boldsymbol{\epsilon}^{pl}, \tag{2.19}$$

is assumed where $\boldsymbol{\epsilon}^{el}$ and $\boldsymbol{\epsilon}^{pl}$ represent the elastic and plastic strain, respectively. Plastic strains represent permanent deformations and do not contribute to elastic energy storage.

To convert (2.7) to small strains, the term $\boldsymbol{P} : \dot{\boldsymbol{F}}$ is replaced by $\boldsymbol{\sigma} : \dot{\boldsymbol{\epsilon}}$. Assuming that the strain energy density depends on the elastic strains $\boldsymbol{\epsilon}^{el}$ and the strain-like internal

variables $\boldsymbol{q}_\alpha$, the mechanical dissipation (2.7) becomes

$$\begin{aligned}\mathcal{D}_{mech} &= \boldsymbol{\sigma} : \dot{\boldsymbol{\epsilon}} - \rho_o \frac{\partial \psi}{\partial \boldsymbol{\epsilon}^{el}} : \dot{\boldsymbol{\epsilon}}^{el} - \rho_o \frac{\partial \psi}{\partial \boldsymbol{q}_\alpha} : \dot{\boldsymbol{q}}_\alpha \\ &= \boldsymbol{\sigma} : \dot{\boldsymbol{\epsilon}}^{pl} - \rho_o \frac{\partial \psi}{\partial \boldsymbol{q}_\alpha} : \dot{\boldsymbol{q}}_\alpha + \left(\boldsymbol{\sigma} - \rho_o \frac{\partial \psi}{\partial \boldsymbol{\epsilon}^{el}} \right) : \dot{\boldsymbol{\epsilon}}^{el} \geq 0,\end{aligned} \tag{2.20}$$

which shows that $\boldsymbol{\sigma} = \rho_o \frac{\partial \psi}{\partial \boldsymbol{\epsilon}^{el}}$ using the arguments of the Coleman-Noll procedure which states that the mechanical dissipation should be fulfilled for any thermodynamic state.

For linear elasticity, assuming isotropic and homogeneous material, the strain energy density function

$$\rho_o \psi = \frac{1}{2} \boldsymbol{\epsilon}^{el} : \mathbb{D}_L : \boldsymbol{\epsilon}^{el} + \rho_o \psi_{\boldsymbol{q}_\alpha} \left(\boldsymbol{q}_\alpha \right), \tag{2.21}$$

can be considered where $\mathbb{D}_L$ is the linear fourth-order elasticity tensor. Consequently, the stress-strain relationship is

$$\boldsymbol{\sigma} = \kappa \mathrm{tr} \left(\boldsymbol{\epsilon}^{el} \right) \boldsymbol{I} + 2\mu \boldsymbol{e}^{el} = \mathbb{D}_L : \boldsymbol{\epsilon}^{el}, \tag{2.22}$$

where $\boldsymbol{e}^{el} = \mathrm{dev} \left(\boldsymbol{\epsilon}^{el} \right)$ the deviatoric elastic strain. Since the potential function ψ does not determine the plastic flow $\dot{\boldsymbol{\epsilon}}^{pl}$, additional constitutive assumptions, such as a yield criterion, is required for the mechanical dissipation (2.20) to be fulfilled.

Papers C, D and E utilize the von-Mises yield criterion

$$f \left(\boldsymbol{\xi}, R \right) = ||\boldsymbol{\xi}|| - \sqrt{\frac{2}{3}} \sigma_y \left(R \right), \tag{2.23}$$

where $\sigma_y = \sigma_{y0} + R$ is the current flow stress, R the isotropic drag stress and σ_{y0} the initial flow stress. The relative stress $\boldsymbol{\xi} = \boldsymbol{s} - \boldsymbol{\beta}$ is characterized by the deviatoric stress $\boldsymbol{s} = \mathrm{dev} \left(\boldsymbol{\sigma} \right)$ and the back stress $\boldsymbol{\beta}$ used to model kinematic hardening. A general non-linear hardening law for the isotropic drag stress is

$$R \left(\alpha \right) = H\alpha + Y_\infty \left(1 - e^{-\delta \alpha} \right), \tag{2.24}$$

where α is a scalar internal variable, H the linear hardening modulus, Y_∞ the saturation stress of the exponential hardening and δ the saturation exponent. The elastic domain is defined by $f < 0$ and plastic response occurs for $f = 0$.

Assuming that $\boldsymbol{q}_\alpha = \left\{ \alpha, \bar{\boldsymbol{\beta}} \right\}$, where $\bar{\boldsymbol{\beta}}$ is the conjugated strain to the back stress $\boldsymbol{\beta}$, the stored energy due to hardening can be modeled as

$$\rho_o \psi_{\boldsymbol{q}_\alpha} \left(\boldsymbol{q}_\alpha \right) = \frac{1}{2} H \alpha^2 + Y_\infty \left(\alpha + \frac{1}{\delta} e^{-\delta \alpha} \right) + \frac{1}{2} \bar{\boldsymbol{\beta}} : \mathbb{H} : \bar{\boldsymbol{\beta}}, \tag{2.25}$$

which provides $R = \rho_o \frac{\partial \psi}{\partial \alpha}$ and where the 4th-order tensor $\mathbb{H}$ is chosen so that $\boldsymbol{\beta} = \rho_o \frac{\partial \psi}{\partial \bar{\boldsymbol{\beta}}}$. The mechanical dissipation (2.20) now becomes

$$\boldsymbol{\sigma} : \dot{\boldsymbol{\epsilon}}^{pl} - \boldsymbol{\beta} : \dot{\bar{\boldsymbol{\beta}}} - R\dot{\alpha} \geq 0. \tag{2.26}$$

The principle of maximum plastic dissipation states that, among all admissible stress states satisfying the yield criterion $f \leq 0$, the stress states should maximize the plastic dissipation. This can be formulated as a constrained minimization problem of (2.26) as

$$\min_{\boldsymbol{\sigma},\boldsymbol{\beta},R} - \left(\boldsymbol{\sigma} : \dot{\boldsymbol{\epsilon}}^{pl} - \boldsymbol{\beta} : \dot{\bar{\boldsymbol{\beta}}} - R\dot{\alpha} \right) + \gamma f, \tag{2.27}$$

where $\gamma \geq 0$ is the Lagrange multiplier. The solution to (2.27) provides the associative plastic flow rule

$$\dot{\boldsymbol{\epsilon}}^{pl} = \gamma \frac{\partial f}{\partial \boldsymbol{\sigma}}, \tag{2.28}$$

and the associative evolution laws

$$\dot{\alpha} = -\gamma \frac{\partial f}{\partial R} = \gamma \sqrt{\frac{2}{3}}, \tag{2.29}$$

and

$$\dot{\bar{\boldsymbol{\beta}}} = -\gamma \frac{\partial f}{\partial \boldsymbol{\beta}}. \tag{2.30}$$

The conjugated strain $\bar{\boldsymbol{\beta}}$ is assumed to be linearly related to the back stress $\boldsymbol{\beta}$, to provide the Melan-Prager evolution law

$$\dot{\boldsymbol{\beta}} = \frac{2}{3} H \dot{\boldsymbol{\epsilon}}^{pl}, \tag{2.31}$$

for the back stress.

The solution to the minimization problem (2.27) provides (2.28)-(2.31), and is feasible if the Karush-Kuhn-Tucker (KKT) -conditions

$$\gamma f\left(\boldsymbol{\xi}, R\right) = 0, \quad \gamma \geq 0, \quad f\left(\boldsymbol{\xi}, R\right) \leq 0, \tag{2.32}$$

for the plastic multiplier γ are fulfilled.

If only isotropic hardening is considered, $\boldsymbol{\beta}$ is zero and similarly, if only kinematic hardening is considered, α is zero. Including both evolution laws (2.29) and (2.31) provides a mixed isotropic-kinematic hardening model.

Chapter 3

Numerical solution procedures

For numerical implementation, the constitutive continuum relations presented in the previous chapter have to be discretized. The finite element method has been used to numerically solve the boundary value problems and this chapter briefly introduces the finite element formulation of the equilibrium equations and the integration of constitutive laws. In Paper A and B, the numerical solution procedure is based on a Total Lagrangian approach where the discretized finite element equations are formulated in material coordinates. whereas Papers C-E assumes linear elasticity and small strains and therefore only consider the reference configuration. The standard Galerkin finite element method is utilized in all works. More information on the finite element method including element choices and integration schemes can be found in e.g. Zienkiewicz and Taylor (2000) or Bathe (2006).

1 Equilibrium residual equations

The balance laws presented in chapter 2, section 3, are the strong form of the equilibrium equations. The finite element formulation stem from the weak form of these equations and are herein provided.

1.1 Mechanical equations

In the weak form of the equilibrium boundary value problem (2.8) the kinematically admissible $\boldsymbol{u}$ is found such that

$$\int_{\Omega_o} \boldsymbol{S} : \delta \boldsymbol{E} \, \mathrm{dV} - \int_{\partial\Omega_{oN}^{\mathcal{M}}} \bar{\boldsymbol{t}} \cdot \delta \boldsymbol{u} \, \mathrm{dS} = 0, \tag{3.1}$$

is fulfilled for all kinematically admissible $\delta\boldsymbol{u}$. In (3.1), $\delta\boldsymbol{E} = \frac{1}{2}\left((\boldsymbol{\nabla}\delta\boldsymbol{u})^{\mathrm{T}}\boldsymbol{F} + \boldsymbol{F}^{\mathrm{T}}\boldsymbol{\nabla}\delta\boldsymbol{u}\right)$ is the virtual Green Lagrangian strain. The thermo-mechanically coupled discretized finite element formulation for time step n is formulated as the mechanical residual equation

$$\boldsymbol{R}_u^{(n)}\left(\boldsymbol{a}_u^{(n)}, \boldsymbol{a}_\theta^{(n)}\right) = \boldsymbol{f}_{u,int}^{(n)}\left(\boldsymbol{a}_u^{(n)}, \boldsymbol{a}_\theta^{(n)}\right) - \boldsymbol{f}_{u,ext}^{(n)} = \boldsymbol{0}, \tag{3.2}$$

where $\boldsymbol{a}_u$ and $\boldsymbol{a}_\theta$ are the nodal displacement and temperature vectors, respectively, and $\boldsymbol{f}_{u,int}$ and $\boldsymbol{f}_{u,ext}$ corresponds to the internal and external forces computed as

$$\begin{aligned}
\boldsymbol{f}_{u,int}^{(n)} &= \int_{\Omega_o} \boldsymbol{B}_u^{(n)^{\mathrm{T}}} \boldsymbol{S}^{(n)} \,\mathrm{dV}, \\
\boldsymbol{f}_{u,ext}^{(n)} &= \int_{\partial\Omega_{oN}^{\mathcal{M}}} \boldsymbol{N}_u^{\mathrm{T}} \bar{\boldsymbol{t}}^{(n)} \,\mathrm{dS}.
\end{aligned} \tag{3.3}$$

The interpolation function vector $\boldsymbol{N}_u$ is used to interpolate the displacement field $\boldsymbol{u}$ as $\boldsymbol{u} \approx \boldsymbol{N}_u\boldsymbol{a}_u$ and the $\boldsymbol{B}_u = \nabla\boldsymbol{N}_u$ is the incremental strain-displacement matrix. Likewise, the interpolation function vector $\boldsymbol{N}_\theta$ is used to interpolate the temperature field as $\theta \approx \boldsymbol{N}_\theta\boldsymbol{a}_\theta$.

1.2 Thermal equations

Stating that the mechanical dissipation is zero for reversble thermo-elastic processes, and neglecting the Kelvin-Joule effect, the kinematically admissible θ is found from the weak form of the thermal energy balance boundary value problem (2.10), such that

$$\int_{\Omega_o} \delta\theta\rho_o c\dot{\theta} \,\mathrm{dV} - \int_{\Omega_o} \nabla\delta\theta \cdot \boldsymbol{q}_o \,\mathrm{dV} - \int_{\Omega_o} \delta\theta\rho_o r \,\mathrm{dV} + \int_{\partial\Omega_{oN}^{\mathcal{T}}} \delta\theta\bar{q} \,\mathrm{dS} = 0, \tag{3.4}$$

is fulfilled for all kinematically admissible $\delta\theta$. The thermo-mechanically coupled discretized finite element formulation for time step n is formulated as the thermal residual equation

$$\boldsymbol{R}_\theta^{(n)}\left(\boldsymbol{a}_u^{(n)}, \boldsymbol{a}_\theta^{(n)}, \boldsymbol{a}_\theta^{(n-1)}\right) = \boldsymbol{f}_{\theta,int}^{(n)}\left(\boldsymbol{a}_u^{(n)}, \boldsymbol{a}_\theta^{(n)}, \boldsymbol{a}_\theta^{(n-1)}\right) - \boldsymbol{f}_{\theta,ext}^{(n)} = \boldsymbol{0}, \tag{3.5}$$

where the internal and external thermal energy vectors are

$$\begin{aligned}
\boldsymbol{f}_{\theta,int}^{(n)} &= \int_{\Omega_o} \boldsymbol{B}_\theta^{\mathrm{T}} \boldsymbol{q}_o^{(n)} \,\mathrm{dV} + \int_{\Omega_o} \boldsymbol{N}_\theta^{\mathrm{T}} \rho_o c \boldsymbol{N}_\theta \frac{1}{\Delta t^{(n)}} (\boldsymbol{a}_\theta^{(n)} - \boldsymbol{a}_\theta^{(n-1)}) \,\mathrm{dV}, \\
\boldsymbol{f}_{\theta,ext}^{(n)} &= \int_{\Omega_o} \boldsymbol{N}_\theta^{\mathrm{T}} \rho_o r^{(n)} \,\mathrm{dV} - \int_{\partial\Omega_{oN}^{\mathcal{T}}} \boldsymbol{N}_\theta^{\mathrm{T}} \bar{q}^{(n)} \,\mathrm{dS},
\end{aligned} \tag{3.6}$$

with $\boldsymbol{B}_\theta = \nabla \boldsymbol{N}_\theta$ [1]. An implicit backward Euler integration scheme has been used in the relation above to approximate the time derivative on the nodal temperature vector as

$$\dot{\boldsymbol{a}}_\theta^{(n)} \approx \frac{1}{\Delta t^{(n)}} \left(\boldsymbol{a}_\theta^{(n)} - \boldsymbol{a}_\theta^{(n-1)} \right). \tag{3.7}$$

An additional discussion on time integration schemes is provided in chapter 5 in relation to the sensitivity analysis.

1.3 Elasto-plastic equations

Simplifying to small strains and linear kinematics, (3.1) is reformulated as

$$\int_{\Omega_o} \boldsymbol{\sigma} : \delta\boldsymbol{\epsilon} \, \mathrm{dV} - \int_{\partial\Omega_{oN}^{\mathcal{M}}} \bar{\boldsymbol{t}} \cdot \delta\boldsymbol{u} \, \mathrm{dS} = 0, \tag{3.8}$$

where $\delta\boldsymbol{\epsilon} = \frac{1}{2}\left((\nabla\delta\boldsymbol{u})^{\mathrm{T}} + \nabla\delta\boldsymbol{u} \right)$ is the linearized virtual strain.

Determining the stress via (2.22), the elasto-plastic mechanical residual equation is formulated as in (3.2), but with arguments $\boldsymbol{R}_u^{(n)}\left(\boldsymbol{a}_u^{(n)}, \boldsymbol{\epsilon}^{pl(n)}\right)$, and the internal force vector

$$\boldsymbol{f}_u^{(n)}\left(\boldsymbol{a}_u^{(n)}, \boldsymbol{\epsilon}^{pl(n)}\right) = \int_{\Omega_o} \boldsymbol{B}_L^{\mathrm{T}} \boldsymbol{\sigma}^{(n)} \, \mathrm{dV}, \tag{3.9}$$

where $\boldsymbol{B}_L$ is the linear part of $\boldsymbol{B}_u$, cf. De Borst et al. (2012).

Integration of constitutive relations

To determine whether an increment is elastic or plastic one can make use of the trial state

$$\begin{aligned} \boldsymbol{\xi}_{trial}^{(n)} &= \boldsymbol{s}^{(n-1)} + 2\mu\Delta\boldsymbol{e}^{(n)} - \boldsymbol{\beta}^{(n-1)}, \\ R_{trial}^{(n)} &= R^{(n-1)}, \end{aligned} \tag{3.10}$$

wherein the plastic state has been frozen from the state $(n-1) \rightarrow (n)$. As the consistency condition (2.23) should be fulfilled during plastic evolution, $f\left(\boldsymbol{\xi}_{trial}^{(n)}, R_{trial}^{(n)}\right) > 0$ implicates that the increment from the last converged state in equilibrium $(n-1)$ to (n) is elasto-plastic. In that case, numerical integration in each quadrature point of the constitutive laws related to the plastic evolution is required. The implicit backward Euler scheme of (2.28),(2.29) and (2.31), together with the consistency condition,

[1] It is should be noted that equations (3.3) and (3.6) are expressed in Voigt notation.

provides the local plastic residual equations

$$\boldsymbol{c}^{(n)}\left(\boldsymbol{\epsilon}^{(n)}, \boldsymbol{w}^{(n)}, \boldsymbol{w}^{(n-1)}\right) = \begin{cases} \boldsymbol{\epsilon}^{pl\,(n)} - \boldsymbol{\epsilon}^{pl\,(n-1)} - \Delta\gamma^{(n)}\boldsymbol{n}^{(n)} = \boldsymbol{0} \\ \alpha^{(n)} - \alpha^{(n-1)} - \sqrt{\frac{2}{3}}\Delta\gamma^{(n)} = 0 \\ \boldsymbol{\beta}^{(n)} - \boldsymbol{\beta}^{(n-1)} - \frac{2}{3}H\Delta\gamma^{(n)}\boldsymbol{n}^{(n)} = \boldsymbol{0} \\ f\left(\boldsymbol{\xi}^{(n)}, R^{(n)}\right) = 0 \end{cases} \tag{3.11}$$

where $\boldsymbol{n}^{(n)} = \frac{\boldsymbol{\xi}^{(n)}}{||\boldsymbol{\xi}^{(n)}||}$ is the normal vector to the yield surface.

Remark: Using that $\boldsymbol{\xi}^{(n)} = \boldsymbol{s}^{(n)} - \boldsymbol{\beta}^{(n)}$, and the updates of $\boldsymbol{\epsilon}^{pl}$ and $\boldsymbol{\beta}$ in (3.11), the relative stress can be expressed as

$$\boldsymbol{\xi}^{(n)} = \boldsymbol{\xi}^{(n)}_{trial} - \left[2\mu\Delta\gamma^{(n)} + \frac{2}{3}H\Delta\gamma^{(n)}\right]\boldsymbol{n}^{(n)}, \tag{3.12}$$

which together with the normal vector to the yield surface can be used to write

$$\boldsymbol{\xi}^{(n)} = \left|\left|\boldsymbol{\xi}^{(n)}\right|\right|\boldsymbol{n}^{(n)} = \boldsymbol{\xi}^{(n)}_{trial} - \left[2\mu\Delta\gamma^{(n)} + \frac{2}{3}H\Delta\gamma^{(n)}\right]\boldsymbol{n}^{(n)}, \tag{3.13}$$

which after some rearranging provides

$$\boldsymbol{n}^{(n)} = \frac{\boldsymbol{\xi}^{(n)}_{trial}}{\left(\left|\left|\boldsymbol{\xi}^{(n)}\right|\right| + \left[2\mu\Delta\gamma^{(n)} + \frac{2}{3}H\Delta\gamma^{(n)}\right]\right)}. \tag{3.14}$$

Since $\left|\left|\boldsymbol{\xi}^{(n)}\right|\right| = \left|\left|\boldsymbol{\xi}^{(n)}_{trial}\right|\right| - \left[2\mu\Delta\gamma^{(n)} + \frac{2}{3}H\Delta\gamma^{(n)}\right]$ can be shown from (3.12), the unit normal vector $\boldsymbol{n}^{(n)}$ can exclusively be determined from the trial elastic state as

$$\boldsymbol{n}^{(n)} = \frac{\boldsymbol{\xi}^{(n)}_{trial}}{\left|\left|\boldsymbol{\xi}^{(n)}_{trial}\right|\right|}. \tag{3.15}$$

The system (3.11) is solved locally for $\boldsymbol{w}^{(n)} = \left\{\boldsymbol{\epsilon}^{pl\,(n)}, \alpha^{(n)}, \boldsymbol{\beta}^{(n)}, \Delta\gamma^{(n)}\right\}$. However, for coaxial plasticity models where the principal stress- and strain directions remain aligned during the state update, (3.11) can be reduced to the, generally non-linear, scalar equation

$$g\left(\Delta\gamma^{(n)}\right) = \left|\left|\boldsymbol{\xi}^{(n)}_{trial}\right|\right| - 2\mu\Delta\gamma^{(n)} - \frac{2}{3}H\Delta\gamma^{(n)} - \sqrt{\frac{2}{3}}\sigma_y\left(R\left(\alpha_{(i)}\right)\right) = 0, \tag{3.16}$$

which efficiently can be solved for $\Delta\gamma^{(n)}$ using Newton iterations. Once $\Delta\gamma^{(n)}$ is found, the plastic state is trivially updated. This procedure is called the radial return

mapping method (Simo and Hughes (2006)) since it is used to compute the plastic strain increment necessary to return the stress state to the yield surface from the trial stress state. The method is summarized in Algorithm 1.

When solving the elasto-plastic equations, a nested formulation can be assumed where the plastic state has an implicit dependency on the displacements, i.e. $\boldsymbol{w}^{(n)} = \boldsymbol{w}^{(n)}\left(\boldsymbol{a}_u^{(n)}\right)$.

Algorithm 1 Radial Return Algorithm for nonlinear mixed isotropic-kinematic hardening

Compute trial elastic relative stress
$\boldsymbol{e}^{(n)} = \boldsymbol{\epsilon}^{(n)} - \frac{1}{3}\left(\text{tr}\left(\boldsymbol{\epsilon}^{(n)}\right)\right)\boldsymbol{I}$
$\boldsymbol{\xi}_{trial}^{(n)} = 2\mu\left(\boldsymbol{e}^{(n)} - \boldsymbol{\epsilon}^{pl(n-1)}\right) - \boldsymbol{\beta}^{(n-1)}$
$f_{trial}^{(n)} := \left|\left|\boldsymbol{\xi}_{trial}^{(n)}\right|\right| - \sqrt{\frac{2}{3}}\sigma_y\left(R^{(n-1)}\right)$
if $f_{trial}^{(n)} \leq 0$ **then**
  $\boldsymbol{\epsilon}^{pl(n)} := \boldsymbol{\epsilon}^{pl(n-1)}$
  $\alpha^{(n)} := \alpha^{(n-1)}$
  $\boldsymbol{\beta}^{(n)} := \boldsymbol{\beta}^{(n-1)}$
  $\boldsymbol{\sigma}^{(n)} := \kappa\text{tr}\left(\boldsymbol{\epsilon}^{(n)}\right)\boldsymbol{I} + 2\mu\left(\boldsymbol{e}^{(n)} - \boldsymbol{\epsilon}^{pl(n-1)}\right)$
else
  Compute $\boldsymbol{n}^{(n)} = \frac{\boldsymbol{\xi}_{trial}^{(n)}}{||\boldsymbol{\xi}_{trial}^{(n)}||}$
  Find $\Delta\gamma^{(n)}$ *by solving* (3.16)
  Update state
  $\boldsymbol{\epsilon}^{pl(n)} := \boldsymbol{\epsilon}^{pl(n-1)} + \Delta\gamma^{(n)}\boldsymbol{n}^{(n)}$
  $\alpha^{(n)} := \alpha^{(n-1)} + \sqrt{\frac{2}{3}}\Delta\gamma^{(n)}$
  $\boldsymbol{\beta}^{(n)} := \boldsymbol{\beta}^{(n-1)} + \frac{2}{3}H\Delta\gamma^{(n)}\boldsymbol{n}^{(n)}$
  $\boldsymbol{\sigma}^{(n)} := \kappa\text{tr}\left(\boldsymbol{\epsilon}^{(n)}\right)\boldsymbol{I} + 2\mu\left(\boldsymbol{e}^{(n)} - \boldsymbol{\epsilon}^{pl(n-1)}\right) - 2\mu\Delta\gamma^{(n)}\boldsymbol{n}^{(n)}$
end if

Furthermore, linearization of the stress $\boldsymbol{\sigma}^{(n)}$ with respect to the total strain $\boldsymbol{\epsilon}^{(n)}$ provides the algorithmic elasto-plastic tangent stiffness. This procedure requires $\frac{d\Delta\gamma^{(n)}}{d\boldsymbol{\epsilon}^{(n)}}$ and $\frac{d\boldsymbol{n}^{(n)}}{d\boldsymbol{\epsilon}^{(n)}}$, which are obtained from differentiating (3.11) and (3.15). An explicit expression for the consistent elasto-plastic tangent can be found in Simo and Hughes (2006).

2 Linearization

All problems established in the previous section are non-linear, which requires a non-linear solution procedure. In finite element analysis, this is usually employed via a Newton-Raphson procedure, which is presented for a general case below.

2.1 Non-linear solution procedure

The collection of state variables is denoted $\boldsymbol{a}$ (which could be both displacements and temperatures) and the implicitly dependent local state variables $\boldsymbol{w}\left(\boldsymbol{a}\right)$ (e.g. the plastic state variables). A first order implicit time integration scheme provides $\dot{\boldsymbol{a}}^{(n)} = \dot{\boldsymbol{a}}^{(n)}\left(\boldsymbol{a}^{(n)}, \boldsymbol{a}^{(n-1)}\right)$ and $\dot{\boldsymbol{w}}^{(n)} = \dot{\boldsymbol{w}}^{(n)}\left(\boldsymbol{w}^{(n)}, \boldsymbol{w}^{(n-1)}\right)$, which is used to formulate the generally non-linear and path-dependent residual equation for time step (n) as

$$\boldsymbol{R}^{(n)} = \boldsymbol{R}^{(n)}\left(\boldsymbol{a}^{(n)}, \boldsymbol{a}^{(n-1)}, \boldsymbol{W}^{(n)}\left(\boldsymbol{a}^{(n)}\right), \boldsymbol{W}^{(n-1)}\left(\boldsymbol{a}^{(n-1)}\right)\right) = \boldsymbol{0}, \tag{3.17}$$

where $\boldsymbol{W}$ represents the global assembly of all local $\boldsymbol{w}$. Linearizing around $\boldsymbol{a}^{(n)}_{(i)}$, with (i) being the current iterate, provides the system

$$\begin{aligned} \left.\frac{d\boldsymbol{R}^{(n)}}{d\boldsymbol{a}^{(n)}}\right|_{(i)} d\boldsymbol{a}_{(i)} &= -\boldsymbol{R}^{(n)}_{(i)}, \\ \boldsymbol{a}^{(n)}_{(i+1)} &:= \boldsymbol{a}^{(n)}_{(i)} + d\boldsymbol{a}_{(i)}, \end{aligned} \tag{3.18}$$

where $\left.\frac{d\boldsymbol{R}^{(n)}}{d\boldsymbol{a}^{(n)}}\right|_{(i)}$ is the tangent stiffness matrix computed for the current state (i) and $d\boldsymbol{a}_{(i)}$ the state increment used to update the solution. The tangent stiffness matrix is expanded to

$$\boldsymbol{K}^{(n)} = \frac{d\boldsymbol{R}^{(n)}}{d\boldsymbol{a}^{(n)}} = \frac{\partial \boldsymbol{R}^{(n)}}{\partial \boldsymbol{a}^{(n)}} + \frac{\partial \boldsymbol{R}^{(n)}}{\partial \boldsymbol{W}^{(n)}}\frac{\partial \boldsymbol{W}^{(n)}}{\partial \boldsymbol{a}^{(n)}}, \tag{3.19}$$

where the implicit derivative $\frac{\partial \boldsymbol{W}^{(n)}}{\partial \boldsymbol{a}^{(n)}}$, in the elasto-plastic case presented previously, is obtained from differentiating the integrated constitutive relations (3.11). Since the tangent stiffness matrix is consistent with the discretized and integrated plastic variables, it is the consistent elasto-plastic tangent stiffness matrix. If plasticity is not considered, the last term in (3.19) simply vanishes.

2.2 Mixed displacement/pressure element formulation

The plastic deformation is purely isochoric wherefore conventional displacement based finite element modeling is prone to volumetric locking. This issue arises because the

incompressibility constraint imposes an excessive number of constraints on the displacement field, leading to an overly stiff response. To mitigate this, mixed displacement/pressure (u/p) finite elements introduce an additional pressure field as an independent variable, ensuring a more accurate and stable solution, see Bathe (2006). This topic was investigated in topology optimization context by Zhang et al. (2018) under finite and small deformations. In small strain problems, this formulation effectively leads to selective reduced integration, where the volumetric part of the finite element formulation is integrated at a lower order compared to the isochoric part, which will be shown herein.

The pressure in a body Ω can be described by

$$p = -\kappa \epsilon_V, \tag{3.20}$$

where $\epsilon_V = \operatorname{tr}(\boldsymbol{\epsilon})$ is the volumetric strain. The stress can be divided into a volumetric and an isochoric part, i.e. $\boldsymbol{\sigma} = -p\boldsymbol{I} + \boldsymbol{s}$. The first term in (3.8) now becomes

$$\int_\Omega \boldsymbol{\sigma} : \delta\boldsymbol{\epsilon} \, \mathrm{dV} = \int_\Omega \boldsymbol{s} : \delta\boldsymbol{\epsilon} \, \mathrm{dV} - \int_\Omega p\boldsymbol{I} : \delta\boldsymbol{\epsilon} \, \mathrm{dV}, \tag{3.21}$$

where it should be noted that $\boldsymbol{I} : \delta\boldsymbol{\epsilon} = \delta\epsilon_V$ and where $\delta\epsilon_V$ is the virtual volumetric strain. Let $\boldsymbol{B}_V$ denote an operator matrix such that $\epsilon_V = \operatorname{tr}(\boldsymbol{\epsilon}) = \boldsymbol{B}_V \boldsymbol{u}$, and similarly $\delta\epsilon_V = \boldsymbol{B}_V \delta\boldsymbol{u}$. Interpolating the pressure field as $p \approx \boldsymbol{N}_p \hat{\boldsymbol{p}}$, and the displacement field $\boldsymbol{u} \approx \boldsymbol{N}_u \boldsymbol{a}$ provides the residual equation

$$\boldsymbol{r}_u(\boldsymbol{a}, \hat{\boldsymbol{p}}) = \int_\Omega \boldsymbol{B}_L^{\mathrm{T}} \boldsymbol{s} \, \mathrm{dV} - \int_\Omega \boldsymbol{B}_V^{\mathrm{T}} \boldsymbol{N}_p \hat{\boldsymbol{p}} \, \mathrm{dV} - \int_{\partial\Omega} \boldsymbol{N}_u^{\mathrm{T}} \bar{\boldsymbol{t}} \, \mathrm{dS} = \boldsymbol{0}, \tag{3.22}$$

which is now expressed in the two nodal state vectors $\boldsymbol{a}$ and $\hat{\boldsymbol{p}}$. To solve (3.22), an additional equation is required. This missing equation is found from (3.20) which in weak form is formulated as

$$\int_\Omega \left(\frac{p}{\kappa} + \epsilon_V \right) \delta p \, \mathrm{dV} = 0, \tag{3.23}$$

where δp is the virtual pressure. Using the same interpolation for δp as the pressure field provides

$$\boldsymbol{r}_p(\boldsymbol{a}, \hat{\boldsymbol{p}}) = \int_\Omega \boldsymbol{N}_p^{\mathrm{T}} \frac{1}{\kappa} \boldsymbol{N}_p \hat{\boldsymbol{p}} \, \mathrm{dV} + \int_\Omega \boldsymbol{N}_p^{\mathrm{T}} \boldsymbol{B}_V \boldsymbol{a} \, \mathrm{dV} = \boldsymbol{0}. \tag{3.24}$$

The coupled system defined by (3.22) and (3.24) is generally non-linear, and solved by a Newton-Raphson procedure where the linearization around the state $\{\boldsymbol{a}, \hat{\boldsymbol{p}}\} = \{\boldsymbol{a}_{(i)}, \hat{\boldsymbol{p}}_{(i)}\}$ provides the linearized system

$$\begin{bmatrix} \frac{d\boldsymbol{r}_u}{d\boldsymbol{a}} & \frac{d\boldsymbol{r}_u}{d\hat{\boldsymbol{p}}} \\ \frac{d\boldsymbol{r}_p}{d\boldsymbol{a}} & \frac{d\boldsymbol{r}_p}{d\hat{\boldsymbol{p}}} \end{bmatrix}_{(i)} \begin{bmatrix} d\boldsymbol{a} \\ d\hat{\boldsymbol{p}} \end{bmatrix}_{(i)} = - \begin{bmatrix} \boldsymbol{r}_u \\ \boldsymbol{r}_p \end{bmatrix}_{(i)}, \tag{3.25}$$

where the new state is updated as

$$\begin{bmatrix} \boldsymbol{a} \\ \hat{\boldsymbol{p}} \end{bmatrix}_{(i+1)} \leftarrow \begin{bmatrix} \boldsymbol{a} \\ \hat{\boldsymbol{p}} \end{bmatrix}_{(i)} + \begin{bmatrix} d\boldsymbol{a} \\ d\hat{\boldsymbol{p}} \end{bmatrix}_{(i)}. \tag{3.26}$$

The system (3.25) can be reduced using Guyan reduction where the bottom equation is statically condensed into the upper equation. The bottom equation provides

$$\begin{aligned} d\hat{\boldsymbol{p}}_{(i)} &= -\left(\frac{d\boldsymbol{r}_p}{d\hat{\boldsymbol{p}}}\right)^{-1}_{(i)} \left(\left(\frac{d\boldsymbol{r}_p}{d\boldsymbol{a}}\right)_{(i)} d\boldsymbol{a}_{(i)} + \boldsymbol{r}_{p(i)}\right) \\ &= -\left(\frac{d\boldsymbol{r}_p}{d\hat{\boldsymbol{p}}}\right)^{-1}_{(i)} \left(\int_\Omega \boldsymbol{N}_p^{\mathrm{T}} \boldsymbol{B}_V \underbrace{\left(\boldsymbol{a}_{(i)} + d\boldsymbol{a}_{(i)}\right)}_{\boldsymbol{a}_{(i+1)}} \,\mathrm{dV}\right) - \hat{\boldsymbol{p}}_{(i)}. \end{aligned} \tag{3.27}$$

Since the displacement and the pressure are updated according to (3.26), and the linear kinematics implies that $\boldsymbol{B}_V$ is constant, the above relation shows that the updated pressure vector is exclusively determined by the updated displacement vector, which would not be the case for large deformations due to non-linear kinematic relations. The pressure vector can therefore be eliminated from (3.25), which simplifies the numerical implementation.

Inserting (3.27) into the upper equation of (3.25) generates the condensed system

$$\hat{\boldsymbol{K}}_{(i)} d\boldsymbol{a}_{(i)} = -\hat{\boldsymbol{r}}_{(i)} \tag{3.28}$$

where

$$\begin{aligned} \hat{\boldsymbol{K}}_{(i)} &= \left(\left(\frac{d\boldsymbol{r}_u}{d\boldsymbol{a}}\right) - \left(\frac{d\boldsymbol{r}_u}{d\hat{\boldsymbol{p}}}\right)\left(\frac{d\boldsymbol{r}_p}{d\hat{\boldsymbol{p}}}\right)^{-1}\left(\frac{d\boldsymbol{r}_p}{d\boldsymbol{a}}\right)\right)_{(i)} \\ &= \left(\int_\Omega \boldsymbol{B}_L^{\mathrm{T}} \frac{d\boldsymbol{s}}{d\boldsymbol{a}} \,\mathrm{dV} + \int_\Omega \boldsymbol{B}_V^{\mathrm{T}} \boldsymbol{N}_p \left(\boldsymbol{N}_p^{\mathrm{T}} \frac{1}{\kappa} \boldsymbol{N}_p\right)^{-1} \boldsymbol{N}_p^{\mathrm{T}} \boldsymbol{B}_V \,\mathrm{dV}\right)_{(i)}, \end{aligned} \tag{3.29}$$

and

$$\begin{aligned} \hat{\boldsymbol{r}}_{(i)} &= -\left(\boldsymbol{r}_u - \left(\frac{d\boldsymbol{r}_u}{d\hat{\boldsymbol{p}}}\right)\left(\frac{d\boldsymbol{r}_p}{d\hat{\boldsymbol{p}}}\right)^{-1} \boldsymbol{r}_p\right)_{(i)} \\ &= -\left(\int_\Omega \boldsymbol{B}_L^{\mathrm{T}} \boldsymbol{s} \,\mathrm{dV} + \int_\Omega \boldsymbol{B}_V^{\mathrm{T}} \boldsymbol{N}_p \left(\boldsymbol{N}_p^{\mathrm{T}} \frac{1}{\kappa} \boldsymbol{N}_p\right)^{-1} \boldsymbol{N}_p^{\mathrm{T}} \boldsymbol{B}_V \boldsymbol{a} \,\mathrm{dV} - \int_{\partial\Omega} \boldsymbol{N}_u^{\mathrm{T}} \bar{\boldsymbol{t}} \,\mathrm{dS}\right)_{(i)} \end{aligned} \tag{3.30}$$

Since the plastic deformation is purely isochoric, the only non-linear component in $\boldsymbol{a}$ or $\hat{\boldsymbol{p}}$ of the Jacobian matrix in (3.25), is $\frac{d\boldsymbol{r}_u}{d\boldsymbol{a}}$.

In the general case, the condensed system (3.28) is solved for $d\boldsymbol{a}_{(i)}$, which is used to update the pressure vector via $\hat{\boldsymbol{p}}_{(i+1)} = \hat{\boldsymbol{p}}_{(i)} + d\hat{\boldsymbol{p}}_{(i)}$. However, since the updated pressure is determined only by the updated displacement vector as shown in (3.27), the linearized system (3.28) corresponds to a selective reduced integration scheme since the pressure, and thereby the volumetric part, is interpolated in a lower order than the isochoric part.

Several choices of mixed element exists, but the studies included in this thesis that utilizes the mixed element formulation uses mixed 8/1 elements, see Fig 3.1 where the displacement field is interpolated using 8-node trilinear brick elements. The pressure field is interpolated using a single-node constant approximation. This provides the pressure interpolation function vector $\boldsymbol{N}_p = 1$, which simplifies the expressions in (3.29) and (3.30). Furthermore, $\boldsymbol{B}_V$ is used to compute the pressure in the center of the element based on the displacements.

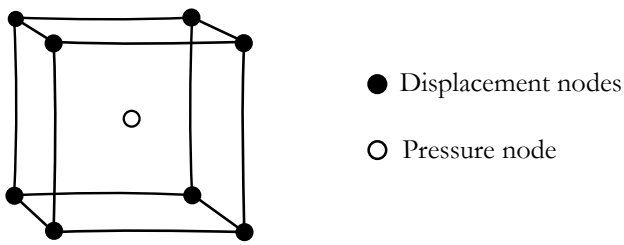

Figure 3.1: Mixed 8/1 u/p element.

Chapter 4

Topology optimization

With the basis of the structural analysis discussed, this chapter aims to introduce the topology optimization frameworks where the finite element analysis is incorporated into gradient-based optimization algorithms. First, regularization via standard filtering and projection methods are discussed followed by material interpolation approaches for single- and multi material optimization. This is followed by a discussion through a simple 1D example on elasto-plastic material interpolation and a free energy interpolation scheme for thermo-hyperelastic materials, used to mitigate numerical instabilities. The chapter ends with a presentation on the optimization problems and some non-trivial optimization objectives that has been considered in this thesis.

1 Regularization and thresholding

In the density-based optimization, the design is defined by the field z, which is piecewise uniform over the finite elements such that one design variable z_e is assigned to each element $e = 1, ..., N_{elm}$ in the mesh where N_{elm} is the number of elements.

It is well known that the density-based topology optimization formulation lacks an intrinsic length scale which causes an ill-conditioned problem via mesh-dependency and numerical defects such as checkerboard patterns. To mitigate this issue and formulate a well-posed optimization problem, restriction by filtration of the design field z is employed to obtain the filtered design field $\tilde{z}$. Several filter techniques exist, including sensitivity filters (Sigmund (1997)), density filters (Bruns and Tortorelli (2001), Bourdin (2001)) or PDE-based filters (Lazarov and Sigmund (2011)), whereas the latter

has been utilized in all studies in this thesis. The (PDE) filter equation is defined by

$$\begin{aligned} -l_o^2 \Delta \tilde{z} + \tilde{z} &= z, \text{ in } \Omega_o, \\ l_o^2 \nabla \tilde{z} \cdot \boldsymbol{n}_o &= -l_s \tilde{z}, \text{ on } \partial\Omega_o, \end{aligned} \tag{4.1}$$

where l_o and l_s are the filter bulk and surface length scales, respectively. The filter equation is solved on the reference configuration using finite elements and Robin boundary conditions are enforced to mitigate undesired boundary effects as shown by Wallin et al. (2018).

A consequence of introducing the filter is diffuse boundaries on the design due to the spatial gradient in the design field. This is usually treated using projection methods (Wang et al. (2011)) where the filtered design field $\tilde{z}$ is thresholded using a Heaviside step function to obtain the physical volume fraction field $\bar{z}$ that controls the constitutive behavior. However, to ensure differentiability, an approximated Heaviside step function

$$\bar{z} = H\left(\tilde{z}\right) = \frac{\tanh\left(\eta\beta\right) + \tanh\left(\beta\left(\tilde{z} - \eta\right)\right)}{\tanh\left(\eta\beta\right) + \tanh\left(\beta\left(1 - \eta\right)\right)}, \tag{4.2}$$

is employed where η is the threshold value and β controls the steepness of the step function approximation. A continuation strategy is commonly applied where β is increased from a small value to a large value throughout the optimization. The sequence of filtering and projection implies the dependency $\bar{z} = \bar{z}\left(\tilde{z}\left(z\right)\right)$. The impact of applying both filtering and projection compared to no restriction is presented in Fig. 4.1.

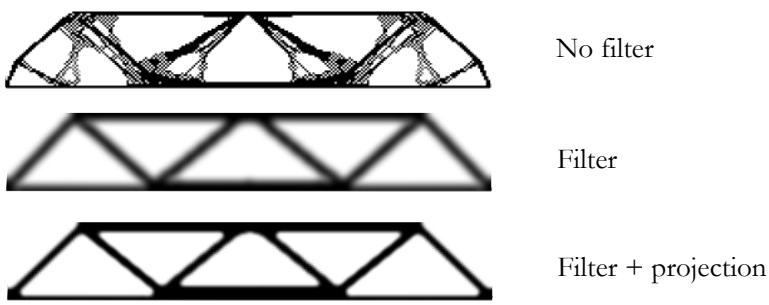

Figure 4.1: Visualization of the impact of using filtering and projection on a benchmark example.

2 Material interpolation

The material properties are formulated as functions of the physical volume fraction field $0 \leq \bar{z} \leq 1$, such that the material property ϕ is interpolated as

$$\phi = \chi\left(\bar{z}\right)\phi_0, \tag{4.3}$$

where χ is the interpolation function and ϕ_0 the bulk material property. The most common interpolation method is the Solid Isotropic Material with Penalization (SIMP) scheme (Bendsøe (1989)) where

$$\chi_S\left(\bar{z}; p, \epsilon_\phi\right) = \epsilon_\phi + \left(1 - \epsilon_\phi\right)\bar{z}^p, \tag{4.4}$$

is used to penalize intermediate density regions by the penalization exponent p so that low density regions provides artificially low material functionality. A small residual value ϵ_ϕ is used to avoid ϕ from becoming zero. The SIMP scheme has zero sensitivity in $\bar{z} = 0$, whereas another popular choice of χ that has a non-zero gradient is the Rational Approximation of Material Properties (RAMP) scheme (Stolpe and Svanberg (2001)) formulated as

$$\chi_R(\xi; q, \epsilon_\phi) = \epsilon_\phi + \frac{\bar{z}\left(1 - \epsilon_\phi\right)}{1 + q(1 - \bar{z})}, \tag{4.5}$$

with the penalization parameter q. A comparison of how (4.4) and (4.5) interpolates the material properties is presented in Fig. 4.2(a).

A generalization of the previously mentioned interpolation functions enables multi material topology optimization (Hvejsel and Lund (2011)). In the case of two solid material phases, an additional design field is introduced such that the combination of $\bar{z}_1$ and $\bar{z}_2$ determines the effective material property. Let μ_0, μ_1 and μ_2 denote the bulk material properties of the "void" material phase one, and the two solid material phases, respectively. The effective material property is then interpolated as

$$\phi(\bar{z}_1, \bar{z}_2; \mu_0, \mu_1, \mu_2) = \mu_0 + \chi(\bar{z}_1; q_1, 0)\left(\mu_1 + \chi(\bar{z}_2; q_2, 0)\left(\mu_2 - \mu_1\right) - \mu_0\right), \tag{4.6}$$

which is visualized for $\chi = \chi_R$, $q_1 = q_2 = 8$ and $\mu_1 = 0.5\mu_2$ in Fig. 4.2(b).

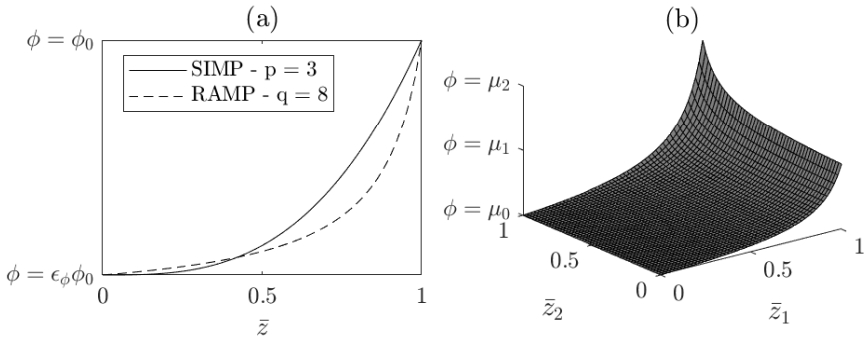

Figure 4.2: (a) Single material interpolation functions and (b) multi material interpolation surface.

Introducing higher values of the penalty parameters increases non-convexity, making the optimization process more complex and challenging to obtain high-quality solutions. To address this, continuation strategies for material interpolation parameters can be employed (Li and Khandelwal (2015)). In this approach, the penalty parameters are gradually increased, starting with a linear interpolation at the beginning of the optimization and transitioning to a non-linear interpolation, see Fig. 4.3. This strategy helps guide the optimization process more effectively, improving convergence and solution quality.

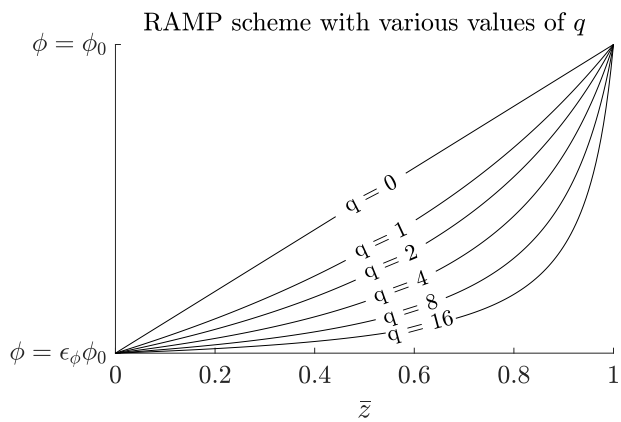

Figure 4.3: Impact on interpolation behavior when applying continuation on the penalty parameters in the RAMP scheme (4.5).

The material interpolation methods for the types of materials used in the studies included in this thesis are presented in the following sections.

Hyperelastic material

For hyperelasticity, the material is described by the bulk- and shear moduli. In the limit of infinitesimal strains, they are determined from the Young's modulus E and Poisson's ratio ν as

$$\kappa = \frac{E}{3(1-2\nu)}, \quad \mu = \frac{E}{2(1+\nu)}, \tag{4.7}$$

and a common approach is to interpolate E so that both κ and μ are interpolated in the same fashion. For most cases ν is kept constant, but for incompressible or nearly incompressible materials, ν can be interpolated so that "void" regions are modeled as compressible (Zhang et al. (2018)). To avoid an ill-conditioned stiffness matrix, a residual value $\epsilon_\phi \sim 10^{-9}$ is enforced in (4.4) or (4.5).

Thermo-hyperelastic material

For transient thermo-elasticity, multiple material parameters are involved and interpolated. The bulk and shear moduli describe the stiffness properties, while the thermal conductivity κ_c and the volumetric heat capacity $\rho_o c$ model the thermal behavior. The thermo-mechanical coupling is introduced via the term $\kappa\alpha_{th}$, known as the thermal stress coefficient.

The material properties mentioned above can be interpolated in various ways and assigning material interpolation parameters requires significant effort. Applying continuation to the penalty parameters can yield satisfactory results and provide insight into the impact of the penalty parameters on the different material properties.

Elasto-plastic material

The elasto-plastic material is described by the elastic material properties κ and μ, and the plastic material properties which are the initial flow stress σ_{y0}, and the hardening parameters that governs the isotropic and kinematic hardening, H and Y_∞ in (2.24).

The interpolation of the elasto-plastic material properties may have a significant impact on the optimized design and the numerical stability in the structural analysis (Pedersen (2002)). A simple one-dimensional example is provided herein to demonstrate issues that arise during elasto-plastic topology optimization.

Consider a specimen subject to a tensile stress σ as illustrated in Fig. 4.4. The stress is related to the elastic tensile strain via

$$\sigma = E\left(\epsilon - \epsilon^{pl}\right), \tag{4.8}$$

and for simplicity only linear isotropic hardening is assumed.

Figure 4.4: Specimen subject to a tensile stress σ.

Plastic strains are developed following the yield criterion

$$f = \sigma - \sigma_{y0} - H\epsilon^{pl} = 0, \tag{4.9}$$

which together with (4.8) provides the incremental elasto-plastic tangent

$$\frac{d\sigma}{d\epsilon} = \frac{EH}{E+H}. \tag{4.10}$$

Going forward, the interpolated material parameters are denoted $\tilde{(\cdot)} = \chi(\bar{z})(\cdot)$. Now, two scenarios are considered when discussing the material interpolation, pre- and post yielding. Before yielding occur, the stress is governed by $\sigma = \tilde{E}\epsilon$ since no plastic strains are present. When the initial flow stress $\tilde{\sigma}_{y0}$ is reached, the corresponding yield strain $\tilde{\epsilon}_{y0}$, is

$$\tilde{\epsilon}_{y0} = \frac{\tilde{\sigma}_{y0}}{\tilde{E}} = \frac{\chi(\bar{z}; p_\sigma, \epsilon_\sigma)\,\sigma_{y0}}{\chi(\bar{z}; p_E, \epsilon_E)\,E}, \tag{4.11}$$

which is highly dependent on the interpolation parameters set for σ_{y0} and E. To avoid massive plastic deformation in low density regions, it is suggested to interpolate σ_{y0} and E so that ϵ_{y0} is artificially high for $\bar{z} \approx 0$, which is obtained for $p_\sigma \leq p_E$ and $\epsilon_E < \epsilon_\sigma$. The initial yield strain is plotted for different values of p_σ in Fig. 4.5, with $p_E = 3$ and $\epsilon_\sigma = \epsilon_E \cdot 10^3$, when using the SIMP scheme (4.4).

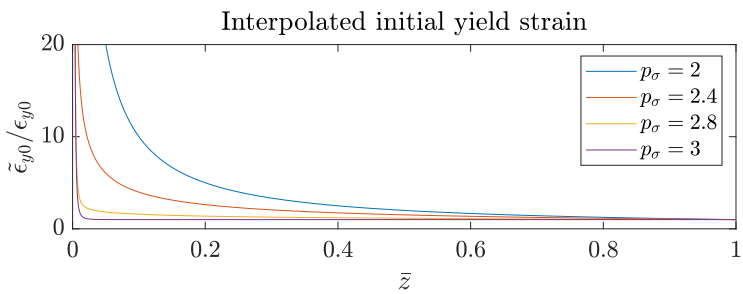

Figure 4.5: Initial yield strain when interpolating the initial flow stress σ_{y0} and Young's modulus E in different ways.

Focusing on the post yielding phase, the stiffness of the material changes from E to the elasto-plastic tangent in (4.10), which provides the interpolated tangent

$$\frac{\chi(\bar{z}; p_E, \epsilon_E)\,\chi(\bar{z}; p_H, \epsilon_H)\,EH}{\chi(\bar{z}; p_E, \epsilon_E)\,E + \chi(\bar{z}; p_H, \epsilon_H)\,H} = \tilde{E}_P, \tag{4.12}$$

which is shown in Fig. 4.6 for the SIMP scheme (4.4) with various values of p_H, $p_E = 3$ and $\epsilon_E = \epsilon_H$. For reference, the interpolated elasto-plastic tangent is compared to the non-interpolated tangent $E_P = \frac{EH}{E+H}$.

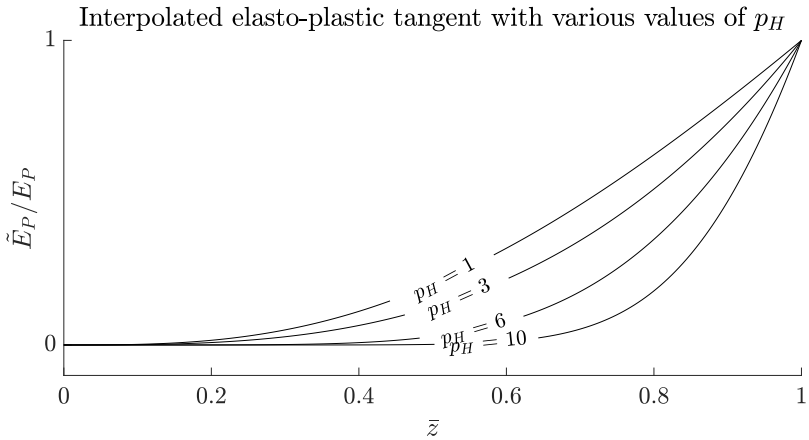

Figure 4.6: Uniaxial interpolated elasto-plastic tangent for different p_H and $p_E = 3$, $\epsilon_E = \epsilon_H$.

To preserve consistency when going from the elastic regime to the plastic regime, one should use $p_E = p_H$ and $\epsilon_E = \epsilon_H$. However, depending on the optimization target, other choices might improve convergence of the solution, and thus, a parameter study is always recommended.

2.1 Discreteness penalization

For some design problems, e.g. mechanical response tailoring, the volume constraint might not be active and material penalization might not be sufficient to obtain a binary and distinct designs. In those cases one can impose a discreteness penalization (Borrvall and Petersson (2001b), Thillaithevan et al. (2024)) via the term

$$d_M\left(\bar{z}; q_d\right) = \frac{1}{|\Omega|} \int_\Omega 4^{q_d} \left(\bar{z} + \delta_d\right)^{q_d} \left(1 - \left(\bar{z} - \delta_d\right)\right)^{q_d} \, \mathrm{dV}, \tag{4.13}$$

where q_d is a penalization exponent and δ_d a small value so that the function is differentiable at the upper and lower bounds of $\bar{z}$. Starting with $q_d = 1$, and then decreasing it via continuation throughout the optimization helps to push intermediate density regions towards zero or one. The discreteness penalization function (4.13) is plotted for decreasing values of q_d in Fig. 4.7.

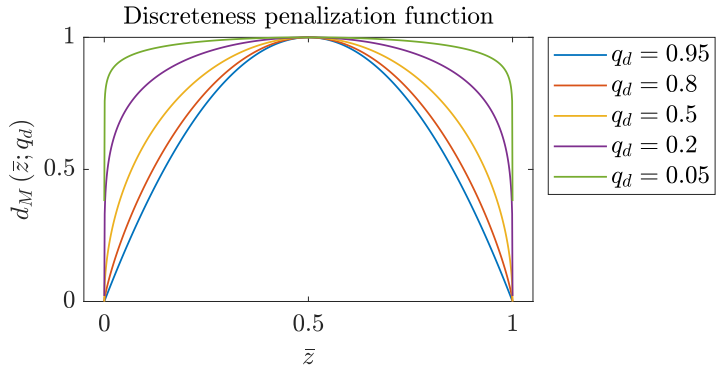

Figure 4.7: Discreteness penalization function with various values of q_d and $\delta_d = 10^{-9}$.

The cost function g can be extended by (4.13) to provide the augmented function

$$\tilde{g} = g + \zeta d_M, \tag{4.14}$$

where ζ is a constant penalty factor, or added as a constraint in the optimization problem.

3 Free energy interpolation scheme for thermo-hyperelasticty

In regions where $\bar{z} \approx 0$, the material stiffness is low, which can lead to excessive deformations. This, in turn, causes highly distorted elements, potentially leading to loss of convergence in the finite element analysis. To mitigate this issue, the strain energy can be interpolated such that low-density regions are modeled as linear elastic (Wang et al. (2014)), thereby stabilizing the structural analysis. This approach can be extended to thermo-elasticity by interpolating the free energy, ensuring a smooth transition from the physical free energy $\psi(\boldsymbol{C}, \theta)$ (2.14) to the linear free energy

$$\psi_L(\boldsymbol{\epsilon}, \theta) = \frac{1}{2}(\boldsymbol{\epsilon} - \boldsymbol{\epsilon}^\theta) : \mathbb{D}_L : (\boldsymbol{\epsilon} - \boldsymbol{\epsilon}^\theta), \tag{4.15}$$

in low-density regions, where $\boldsymbol{\epsilon}^\theta = \alpha_{th}\,(\theta - \theta_0)\,\boldsymbol{I}$ represents the thermal strains. The transitioned free energy ψ_T is computed by applying an interpolation function ξ to the displacement gradient $\nabla \boldsymbol{u}$ such that

$$\psi_T(\nabla \boldsymbol{u}, \theta, \xi) = \psi(\boldsymbol{C}(\xi \nabla \boldsymbol{u}), \theta) + \psi_L(\boldsymbol{\epsilon}, \theta) - \psi_L(\boldsymbol{\epsilon}(\xi \nabla \boldsymbol{u}), \theta), \tag{4.16}$$

where $\xi = H\,(\chi\,(\bar{z}))$ is the approximated Heaviside step function in (4.2), but with input χ to ensure the transition is based on the interpolation of stiffness-related material properties.

A consequence of (4.16)) is that the mechanical internal force vector becomes

$$\hat{\boldsymbol{f}}_{u,int}^{(n)} = \xi \boldsymbol{f}_{u,int}^{(n)} \left(\xi \boldsymbol{a}_u^{(n)}, \boldsymbol{a}_\theta^{(n)} \right) + \tilde{\boldsymbol{f}}_L^{(n)} \left(\boldsymbol{a}_u^{(n)}, \boldsymbol{a}_\theta^{(n)}, \xi \right), \tag{4.17}$$

where $\boldsymbol{f}_{u,int}^{(n)}$ is defined in (3.3), and

$$\tilde{\boldsymbol{f}}_L^{(n)} \left(\boldsymbol{a}_u^{(n)}, \boldsymbol{a}_\theta^{(n)}, \xi \right) = \int_{\Omega_o} \left(\boldsymbol{B}_L^{\mathrm{T}} \boldsymbol{\sigma}_L^{(n)} \left(\boldsymbol{a}_u^{(n)}, \boldsymbol{a}_\theta^{(n)} \right) - \xi \boldsymbol{B}_L^{\mathrm{T}} \boldsymbol{\sigma}_L^{(n)} \left(\xi \boldsymbol{a}_u^{(n)}, \boldsymbol{a}_\theta^{(n)} \right) \right) \, \mathrm{dV}, \tag{4.18}$$

where $\boldsymbol{\sigma}_L$ represents the linear elastic stress. This formulation ensures that when $\xi = 1$, the internal forces are based on the physical free energy ψ, whereas when $\xi = 0$, they are derived from the linear strain energy ψ_L.

Similarly, the internal thermal energy vector follows the formulation in (3.6), but with the heat flux vector modified as

$$\boldsymbol{q}_o^{(n)} \left(\xi \boldsymbol{a}_u^{(n)}, \boldsymbol{a}_\theta^{(n)} \right) = -J_\xi \boldsymbol{F}_\xi^{-1} \boldsymbol{\kappa}_c \boldsymbol{F}_\xi^{-\mathrm{T}} \boldsymbol{B}_\theta \boldsymbol{a}_\theta^{(n)}, \tag{4.19}$$

where $\boldsymbol{F}_\xi$ and J_ξ denotes that the deformation gradient and it's determinant are computed with the displacement gradient $\xi \nabla \boldsymbol{u}$. This extension was specifically developed for designing thermal actuators, where low-density regions could exhibit large compressions that caused numerical instabilities and convergence issues. The proposed free energy transition scheme significantly improved the stability of the analysis, with good performance achieved using $\beta = 500$ and $\eta = 0.05$ in the interpolation function ξ.

4 Optimization formulation

The optimization problems studied in this thesis are formulated as mathematical programming problems by considering the minimization of a cost function g, subject to inequality constraints $g_i \leq 0$ and box constraints $0 \leq z_e \leq 1$, where $i = 1, ..., N_c$ is the number of inequality constraints, and $e = 1, ..., N_{elm}$. Furthermore, the structural equilibrium equations should be fulfilled which introduces the equality constraints $\boldsymbol{R}^{(n)} = \boldsymbol{0}$ for each time step $n = 1, ..., N$ where N is the total number of steps. Altogether, this renders the optimization formulation

$$(\mathbb{TO}) \begin{cases} \min\limits_{\boldsymbol{z}} & g \\ \text{s.t} \begin{cases} & g_i \leq 0, \ i = 1, ..., N_c \\ & \boldsymbol{R}^{(n)} = \boldsymbol{0}, \ n = 1, ..., N \\ & 0 \leq z_e \leq 1, \ e = 1, ..., N_{elm} \end{cases} \end{cases} \tag{4.20}$$

The optimization problem (4.20) is solved by first ensuring that $\boldsymbol{R}^{(n)} = \boldsymbol{0}$ are fulfilled for the given design field $\boldsymbol{z}$, and then the responses are used to compute the cost and constraint functions, and their gradients.

4.1 Non-trivial cost- and constraint functions

Below follows some examples on how to formulate some challenging cost- and constraint functions together with a discussion on when they might be desirable.

Stress constraints for non-proportional loading

Stress constraints has been investigated in the context of topology optimization for many years. Still, research on this matter is ongoing.

In Paper A, hyperelastic structures subjected to non-proportional loading were investigated. In such cases, the stress must be considered at every spatial and temporal point throughout the body, since the location of peak stress is not known in advance. This can potentially lead to an extremely large number of stress constraints, necessitating the use of an efficient constrained optimization method. Traditionally, stress constraints are handled using aggregation techniques such as the P-norm Le et al. (2010) or the Kreisselmeier–Steinhauser function Verbart et al. (2017), where the peak stress is approximated by a single differentiable function that captures the stress behavior across the entire structure. An alternative approach is the augmented Lagrangian method da Silva et al. (2021), in which the stress at each point is incorporated into a Lagrangian function that is minimized.

The von Mises equivalent stress is in each quadrature point gp and load step n formulated in terms of the deviatoric stress as

$$\sigma_{eff,gp}^{(n)} = \left(\frac{3}{2} \boldsymbol{s}_{gp}^{(n)} : \boldsymbol{s}_{gp}^{(n)} \right)^{\frac{1}{2}} \tag{4.21}$$

which is constrained as

$$g_{gp}^{(n)} = \frac{\sigma_{eff,gp}^{(n)}}{\bar{\sigma}} - 1 \leq 0, \quad gp = 1, ..., N_{gp}, \; n = 1, ..., N, \tag{4.22}$$

where N_{gp} is the number of quadrature points and N the number of load steps. Constraining each point throughout the load trajectory results in $N_{gp} \cdot N$ stress constraints.

The Lagrangian function is formulated by augmenting the original cost function g with each constraint multiplied by a penalty parameter μ_σ and Lagrange multipliers λ_σ as

$$\mathcal{L} = g + \frac{\mu_\sigma}{2} \sum_{n=1}^{N} \left(\sum_{gp=1}^{N_{gp}} \left\langle \frac{\lambda_{\sigma,gp}^{(n)}}{\mu_\sigma} - g_{gp}^{(n)} \right\rangle^2 \right) \tag{4.23}$$

where $\langle \cdot \rangle$ is the Macaulay bracket. A sequence of subproblems are solved with fixed value of the penalty parameter, which is then increased after each subproblem is deemed

converged. The Lagrange multipliers are updated throughout the optimization as

$$\lambda_{\sigma,gp}^{(n)} \leftarrow \left\langle \lambda_{\sigma,gp}^{(n)} + \mu_\sigma g_{gp}^{(n)} \right\rangle . \tag{4.24}$$

A benefit of using the augmented Lagrangian method is that the stress constraint is enforced with a chosen limit in each point in the simulations. This approach however, requires more parameter tuning for optimal performance compared to e.g. aggregation methods.

In the numerical simulations investigated in Paper A, each subproblem was deemed converged after 50 design iterations, and the Lagrange multipliers was updated according to (4.24) every 5^{th} design iteration.

Accounting for the entire load history in the optimization generates significantly different optimized designs depending on the load path since the optimization formulation, per definition, is path-dependent. However, it should be noted that the state problem is not path-dependent, which simplifies the sensitivity analysis compared to e.g. an elasto-plastic constitutive model.

The singularly problem is a well-known challenge in stress constrained topology optimization problems. The issue arises due to stress constraints becoming ill-defined in low density regions due to stiffness interpolation using e.g. SIMP (4.4). Since the stress is proportional to the stiffness interpolation, i.e. $\sigma \propto \chi\left(\bar{z}; p_E\right)$, the physically consistent stress constraint should be formulated as

$$\sigma - \chi\left(\bar{z}; p_E\right) \bar{\sigma} \leq 0 \iff \frac{\sigma}{\chi\left(\bar{z}; p_E\right)} - \bar{\sigma} \leq 0, \tag{4.25}$$

where $\bar{\sigma}$ is the equivalent stress limit. This choice provides a discontinuity in the stress constraint as $\bar{z} \to 0$. To mitigate this singularity issue, one can make use of ϵ-relaxation methods (Cheng and Guo (1997)) or the commonly employed q/p-approach proposed by Bruggi (2008) where the equivalent stress limit $\bar{\sigma}$ is regularized using a different penalty parameter q_σ such that the stress constraint limit is $\chi_\sigma\left(\bar{z}; q_\sigma\right) \bar{\sigma}$. Choosing $q_\sigma < p_E$ ensures that the stress is "relaxed" in intermediate regions, and gives no discontinuity of local stress as $\bar{z} = 0$.

Self locking structures and reversed loading

Compliant mechanisms are a well-studied topic in topology optimization. Self-locking structures, however, differ in that they involve reversed loading and focus on the unloaded, permanently deformed state as the optimization target. To accurately capture the mechanical response over an entire load cycle, kinematic hardening must be considered to model the Bauschinger effect.

Self-locking mechanisms are typically one-time-use devices where the structure, after unloading, should retain a desirable, permanently deformed state. An example is a fastening mechanism that functions as a gripper. The gripper is first loaded and then unloaded, and after unloading, it should maximize the gripping force at a specific location (see Fig. 4.8). Designing such a mechanism requires intentionally inducing plastic strains and incorporating them into the optimization framework.

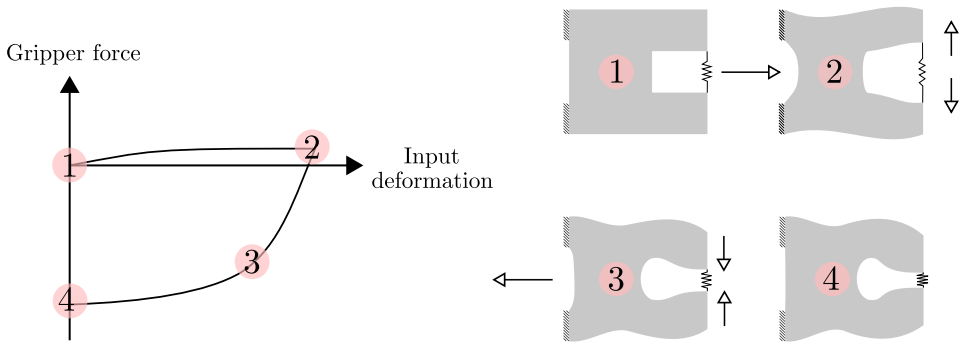

Figure 4.8: Load cycle for a fastening mechanism: undeformed state (1), fully onloaded state (2), unloaded state (3), original position (4) with permanent deformations. Arrows indicate directions of movement.

In contrast to monotone or proportional loading, where normal interaction with the workpiece is often modeled using linear springs, self-locking grippers exhibit opposing movements during loading and unloading. To accurately model the interaction with the gripped workpiece, the interaction with the workpiece needs to be modeled. However, since the contact regions are predetermined in the design problem, a smooth traction-separation law can be introduced to describe the interaction. This law should provide nearly zero stiffness when the work piece is not being gripped, and constant stiffness during compression. One such model is given by

$$t_n(\delta) = \frac{k_0}{2}\left(\delta - \frac{1}{c}\ln\left(\cosh\left(c\cdot\delta\right)\right)\right), \tag{4.26}$$

where δ represents the deformation (compression for $\delta < 0$), k_0 controls the stiffness and c governs the steepness of the transition around $\delta = 0$. The behavior the model (4.26) is shown in Fig. 4.9 for $k_0 = 500$ GPa and various values of c with a reference curve that represents the desirable behavior.

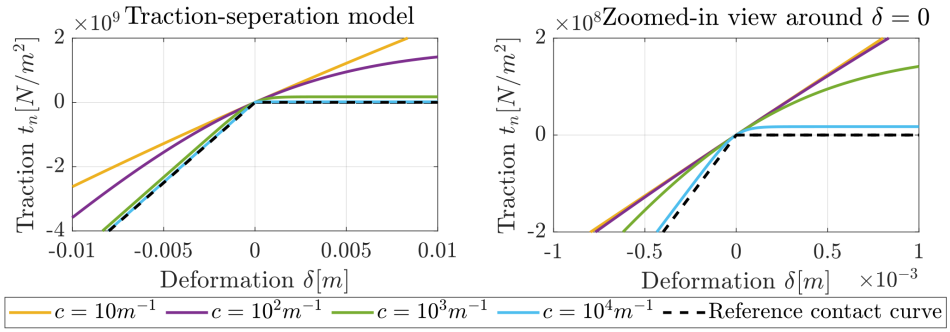

Figure 4.9: Traction-separation model function vs. deformation.

This simple yet effective approach to simulate interaction with the workpiece was investigated in Paper D. With the model established, the objective function is straightforwardly formulated as maximizing either the output displacement or the gripping force at the contact location.

Elasto-plastic end tangent stiffness

A popular objective for topology optimization is to minimize the end compliance, which corresponds to displacement minimization. This stiffness definition corresponds to the secant stiffness which is defined by the displacement for a given load. However, for non-linear material responses, the "stiffness" definition is not uniquely defined. A more intuitive stiffness measure would be the end tangent stiffens, which has been investigated by Kemmler et al. (2005) and Wallin et al. (2018) for non-linear kinematics and elastic materials. The same idea can be applied to elasto-plastic materials. The tangent stiffness and the secant stiffness is illustrated in Fig. 4.10.

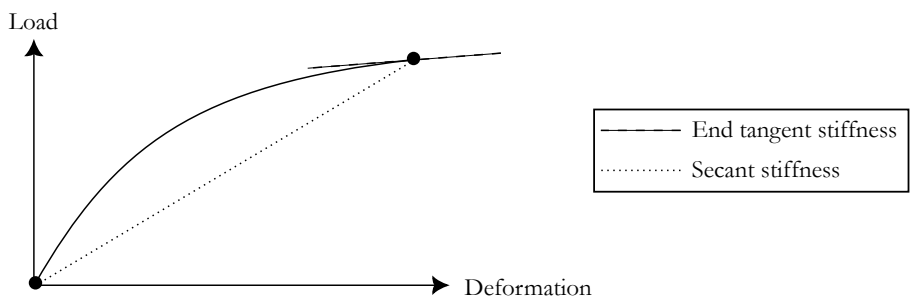

Figure 4.10: Illustration of tangent stiffness (dashed lines) and secant stiffness (dotted line).

To formulate the end-tangent stiffness cost function, displacement controlled loading is considered where the displacement magnitude level for load step n is $\lambda_L^{(n)}$. Let $\boldsymbol{P}$ be a vector corresponding to the degrees of freedom with prescribed displacement such that $\boldsymbol{a}_p^{(n)} = \lambda_L^{(n)} \boldsymbol{P}$. The displacement vector for the free degrees of freedom is denoted $\boldsymbol{a}_f^{(n)}$ so that the total displacement vector is $\boldsymbol{a}^{(n)} = \begin{bmatrix} \boldsymbol{a}_f^{(n)} & \boldsymbol{a}_p^{(n)} \end{bmatrix}$. It follows that $\boldsymbol{a}_f^{(n)}$ has an implicit dependency on the displacement magnitude level, i.e. $\boldsymbol{a}_f^{(n)} = \boldsymbol{a}_f^{(n)}\left(\lambda_L^{(n)}\right)$. The total reaction force corresponding to the displacement magnitude $\lambda_L^{(n)}$ is

$$F_p^{(n)} = \boldsymbol{P}^{\mathrm{T}} \boldsymbol{f}_{p,ext}^{(n)}, \tag{4.27}$$

where $\boldsymbol{f}_{p,ext}^{(n)}$ is the external reaction force vector in the prescribed degrees of freedom. Equilibrium requires $\boldsymbol{f}_{p,ext}^{(n)} = \boldsymbol{f}_{p,int}^{(n)}$, so that the tangent stiffness at load step n is quantified as

$$\begin{aligned} g_T^{(n)} &= \frac{dF_p^{(n)}}{d\lambda_L^{(n)}} = \boldsymbol{P}^{\mathrm{T}} \frac{d\boldsymbol{f}_{p,int}^{(n)}}{d\boldsymbol{a}_f^{(n)}} \frac{d\boldsymbol{a}_f^{(n)}}{d\lambda_L^{(n)}} + \boldsymbol{P}^{\mathrm{T}} \frac{d\boldsymbol{f}_{p,int}^{(n)}}{d\boldsymbol{a}_p^{(n)}} \frac{\partial \boldsymbol{a}_p^{(n)}}{\partial \lambda_L^{(n)}} \\ &= \boldsymbol{P}^{\mathrm{T}} \left(\boldsymbol{K}_{pf}^{(n)} \boldsymbol{v}_f^{(n)} + \boldsymbol{K}_{pp}^{(n)} \boldsymbol{P} \right), \end{aligned} \tag{4.28}$$

which should be maximized. Above, it was used that the tangent stiffness matrix can be partitioned as

$$\boldsymbol{K}^{(n)} = \frac{d\boldsymbol{f}_{int}^{(n)}}{d\boldsymbol{a}^{(n)}} = \begin{bmatrix} \boldsymbol{K}_{ff}^{(n)} & \boldsymbol{K}_{fp}^{(n)} \\ \boldsymbol{K}_{pf}^{(n)} & \boldsymbol{K}_{p}^{(n)} \end{bmatrix}. \tag{4.29}$$

To compute $\boldsymbol{v}_f^{(n)} = \frac{d\boldsymbol{a}_f^{(n)}}{d\lambda_L^{(n)}}$, defined in (4.28), the equilibrium residual vector related to the free degrees of freedoms, $\boldsymbol{R}_f^{(n)}$ is linearized around $\lambda_L^{(n)}$ to obtain

$$\boldsymbol{H}^{(n)} = \frac{d\boldsymbol{R}_f^{(n)}}{d\boldsymbol{a}_f^{(n)}} \frac{d\boldsymbol{a}_f^{(n)}}{d\lambda_L^{(n)}} + \frac{d\boldsymbol{R}_f^{(n)}}{d\boldsymbol{a}_p^{(n)}} \frac{\partial \boldsymbol{a}_p^{(n)}}{\partial \lambda_L^{(n)}} = \boldsymbol{K}_{ff}^{(n)} \boldsymbol{v}_f^{(n)} + \boldsymbol{K}_{fp}^{(n)} \boldsymbol{P} = \boldsymbol{0}, \tag{4.30}$$

which is solved for $\boldsymbol{v}_f^{(n)}$.

In paper E it is shown that structures optimized for maximized secant stiffness under a elasto-plastic response might be near to collapse as the end tangent stiffness is low at the terminal load step. Using the proposed end tangent stiffness formulation provides structures with lower secant stiffness, but larger end tangent stiffness.

Chapter 5

Path-dependent sensitivity analysis

Due to the path-dependent state problem, the sensitivity analysis will be path-dependent too, which indeed adds complexity. To derive a fully consistent discrete adjoint sensitivity analysis, the discretize-then-differentiate approach (Michaleris et al. (1994), Jensen et al. (2014)) is employed where the gradients are calculated on the integrated, and discretized equilibrium equations. This chapter provides the derivation of a transient thermo-mechanically coupled, and path-dependent elasto-plastic problem.

1 Coupled and path-dependent residual formulation

Let $\boldsymbol{a}(t)$ denote the nodal state variables of a discretized system, e.g. displacements and temperatures, that are time dependent. Furthermore, the assembly of all Gauss-point plastic variables $\boldsymbol{w} = \boldsymbol{w}(\boldsymbol{a})$ are collected in $\boldsymbol{W}$. The finite element formulation of the governing equations can be stated as

$$\boldsymbol{M}\dot{\boldsymbol{a}} = \boldsymbol{f}\left(\boldsymbol{a}(t), \boldsymbol{W}(t, \boldsymbol{a}(t))\right), \tag{5.1}$$

where $\boldsymbol{M}$ is a matrix that arises from the time derivative term in the weak formulation, and $\boldsymbol{f}$ is the right-hand-side of the equations. As shown in chapter 2, evolution of $\boldsymbol{W}$ are formulated as

$$\dot{\boldsymbol{W}} = \boldsymbol{g}\left(\boldsymbol{a}(t), \boldsymbol{W}(t, \boldsymbol{a}(t))\right), \tag{5.2}$$

where $\boldsymbol{g}$ contains constitutive equations. Equations (5.1) and (5.2) constitutes the coupled and path-dependent residual formulation

$$\begin{cases} \boldsymbol{R} = \boldsymbol{M}\dot{\boldsymbol{a}} - \boldsymbol{f}\left(\boldsymbol{a}(t), \boldsymbol{W}(t, \boldsymbol{a}(t))\right) = \boldsymbol{0} \\ \boldsymbol{C} = \dot{\boldsymbol{W}} - \boldsymbol{g}\left(\boldsymbol{a}(t), \boldsymbol{W}(t, \boldsymbol{a}(t))\right) = \boldsymbol{0} \end{cases}, \tag{5.3}$$

which are solved for $\boldsymbol{a}$ and $\boldsymbol{W}$. To solve (5.3), the time is discretized which is discussed in the following section.

2 Discretization of path-dependent state variables

Temporal discretization is required to solve (5.3). Integrating (5.1) between times t and $t + \Delta t$ yields

$$\int_t^{t+\Delta t} \boldsymbol{M}\dot{\boldsymbol{a}} \, \mathrm{dt} = \int_t^{t+\Delta t} \boldsymbol{f}\left(\boldsymbol{a}\left(t\right), \boldsymbol{W}\left(t, \boldsymbol{a}\left(t\right)\right)\right) \, \mathrm{dt}, \tag{5.4}$$

where the integrals needs to be approximated. One approach to approximate the integral is to consider a weight between the states at t and $t + \Delta t$, which provides

$$\boldsymbol{M}\left(\boldsymbol{a}\left(t+\Delta t\right) - \boldsymbol{a}\left(t\right)\right) = \left(w_\theta \boldsymbol{f}\left(t+\Delta t\right) - \left(1-w_\theta\right)\boldsymbol{f}\left(t\right)\right)\Delta t, \tag{5.5}$$

where w_θ the weight factor that determines the type of integration method. Choosing $w_\theta = 1$ provides the implicit Euler backward method, $w_\theta = 0$ corresponds to the explicit Euler forward method and $w_\theta = 0.5$ is the Crank-Nicholson method.

In this thesis, the implicit Euler backward integration method has been employed such that (5.3) becomes

$$\begin{cases} \boldsymbol{R}^{(n)} = \boldsymbol{M}\left(\boldsymbol{a}^{(n)} - \boldsymbol{a}^{(n-1)}\right) - \Delta t^{(n)} \boldsymbol{f}\left(\boldsymbol{a}^{(n)}, \boldsymbol{W}^{(n)}\left(\boldsymbol{a}^{(n)}\right)\right) = \boldsymbol{0} \\ \boldsymbol{C}^{(n)} = \boldsymbol{W}^{(n)} - \boldsymbol{W}^{(n-1)} - \Delta t^{(n)} \boldsymbol{g}\left(\boldsymbol{a}^{(n)}, \boldsymbol{W}^{(n)}\left(\boldsymbol{a}^{(n)}\right)\right) = \boldsymbol{0} \end{cases}, \tag{5.6}$$

where superscript n refers to time $t^{(n-1)} + \Delta t^{(n)}$ and $n-1$ to $t^{(n-1)}$.

3 Adjoint sensitivity analysis

The sensitivity analysis is derived from the general cost function g which depends on the states of all time steps $n = 1, ..., N$, as well as the physical volume fraction vector $\bar{\boldsymbol{z}}$, i.e.

$$g = g\left(\bar{\boldsymbol{z}}, \boldsymbol{a}^{(1)}, \boldsymbol{W}^{(1)}, \boldsymbol{a}^{(2)}, \boldsymbol{W}^{(2)}, ..., \boldsymbol{a}^{(N)}, \boldsymbol{W}^{(N)}\right), \tag{5.7}$$

where it is emphasized that the state variables implicitly depend on the design variables such that $\boldsymbol{a}^{(n)} = \boldsymbol{a}^{(n)}\left(\bar{\boldsymbol{z}}\right)$ and $\boldsymbol{W}^{(n)} = \boldsymbol{W}^{(n)}\left(\bar{\boldsymbol{z}}, \boldsymbol{a}^{(n)}\left(\bar{\boldsymbol{z}}\right)\right)$. To compute the gradient of (5.7) with respect to $\bar{\boldsymbol{z}}$, the function is augmented as

$$\tilde{g} = g + \sum_{n=1}^{N} \left(\boldsymbol{\lambda}^{(n)^{\mathrm{T}}} \boldsymbol{R}^{(n)} + \boldsymbol{\gamma}^{(n)^{\mathrm{T}}} \boldsymbol{C}^{(n)}\right), \tag{5.8}$$

where $\boldsymbol{\lambda}^{(n)}$ and $\boldsymbol{\gamma}^{(n)}$ are adjoint vectors. Since $\boldsymbol{R}^{(n)} = \mathbf{0}$ and $\boldsymbol{C}^{(n)} = \mathbf{0}$ in the nested optimization formulation, it follows that $\frac{d\tilde{g}}{d\boldsymbol{z}} = \frac{dg}{d\boldsymbol{z}}$. Likewise, the arguments for $\boldsymbol{R}^{(n)}$ and $\boldsymbol{C}^{(n)}$ are

$$\begin{aligned}\boldsymbol{R}^{(n)} &= \boldsymbol{R}^{(n)}\left(\bar{\boldsymbol{z}}, \boldsymbol{a}^{(n)}, \boldsymbol{a}^{(n-1)}, \boldsymbol{W}^{(n)}, \boldsymbol{W}^{(n-1)}\right), \\ \boldsymbol{C}^{(n)} &= \boldsymbol{C}^{(n)}\left(\bar{\boldsymbol{z}}, \boldsymbol{a}^{(n)}, \boldsymbol{W}^{(n)}, \boldsymbol{W}^{(n-1)}\right).\end{aligned} \tag{5.9}$$

Due to regularization via filtering and projection, as described in chapter 4, section 1, computing $\frac{d\tilde{g}}{d\boldsymbol{z}}$ includes the chain rule contributions

$$\frac{d\tilde{g}}{d\boldsymbol{z}} = \frac{d\tilde{g}}{d\bar{\boldsymbol{z}}}\frac{\partial\bar{\boldsymbol{z}}}{\partial\tilde{\boldsymbol{z}}}\frac{d\tilde{\boldsymbol{z}}}{d\boldsymbol{z}}, \tag{5.10}$$

which are obtained fro differentiating (4.2) and (4.1). Following herein, an approach to find $\frac{d\tilde{g}}{d\bar{\boldsymbol{z}}}$ is sought for.

Differentiating (5.8) with respect to $\bar{\boldsymbol{z}}$ yields

$$\begin{aligned}\frac{d\tilde{g}}{d\bar{\boldsymbol{z}}} = \frac{\partial g}{\partial\bar{\boldsymbol{z}}} &+ \sum_{n=1}^{N}\left(\frac{\partial g}{\partial\boldsymbol{a}^{(n)}}\frac{d\boldsymbol{a}^{(n)}}{d\bar{\boldsymbol{z}}} + \frac{\partial g}{\partial\boldsymbol{W}^{(n)}}\frac{d\boldsymbol{W}^{(n)}}{d\boldsymbol{a}^{(n)}}\frac{d\boldsymbol{a}^{(n)}}{d\bar{\boldsymbol{z}}} + \frac{\partial g}{\partial\boldsymbol{W}^{(n)}}\frac{d\boldsymbol{W}^{(n)}}{d\bar{\boldsymbol{z}}}\right) \\ &+ \sum_{n=1}^{N}\left(\boldsymbol{\lambda}^{(n)\mathrm{T}}\frac{\partial\boldsymbol{R}^{(n)}}{\partial\bar{\boldsymbol{z}}} + \boldsymbol{\lambda}^{(n)\mathrm{T}}\frac{\partial\boldsymbol{R}^{(n)}}{\partial\boldsymbol{a}^{(n)}}\frac{d\boldsymbol{a}^{(n)}}{d\bar{\boldsymbol{z}}} + \boldsymbol{\lambda}^{(n)\mathrm{T}}\frac{\partial\boldsymbol{R}^{(n)}}{\partial\boldsymbol{W}^{(n)}}\frac{d\boldsymbol{W}^{(n)}}{d\boldsymbol{a}^{(n)}}\frac{d\boldsymbol{a}^{(n)}}{d\bar{\boldsymbol{z}}}\right. \\ &\qquad\left. + \boldsymbol{\lambda}^{(n)\mathrm{T}}\frac{\partial\boldsymbol{R}^{(n)}}{\partial\boldsymbol{W}^{(n)}}\frac{d\boldsymbol{W}^{(n)}}{d\bar{\boldsymbol{z}}}\right) \\ &+ \sum_{n=2}^{N}\left(\boldsymbol{\lambda}^{(n)\mathrm{T}}\frac{\partial\boldsymbol{R}^{(n)}}{\partial\boldsymbol{a}^{(n-1)}}\frac{d\boldsymbol{a}^{(n-1)}}{d\bar{\boldsymbol{z}}} + \boldsymbol{\lambda}^{(n)\mathrm{T}}\frac{\partial\boldsymbol{R}^{(n)}}{\partial\boldsymbol{W}^{(n-1)}}\frac{d\boldsymbol{W}^{(n-1)}}{d\boldsymbol{a}^{(n-1)}}\frac{d\boldsymbol{a}^{(n-1)}}{d\bar{\boldsymbol{z}}}\right. \\ &\qquad\left. + \boldsymbol{\lambda}^{(n)\mathrm{T}}\frac{\partial\boldsymbol{R}^{(n)}}{\partial\boldsymbol{W}^{(n-1)}}\frac{d\boldsymbol{W}^{(n-1)}}{d\bar{\boldsymbol{z}}}\right) \\ &+ \sum_{n=1}^{N}\left(\boldsymbol{\gamma}^{(n)\mathrm{T}}\frac{\partial\boldsymbol{C}^{(n)}}{\partial\bar{\boldsymbol{z}}} + \boldsymbol{\gamma}^{(n)\mathrm{T}}\frac{\partial\boldsymbol{C}^{(n)}}{\partial\boldsymbol{a}^{(n)}}\frac{d\boldsymbol{a}^{(n)}}{d\bar{\boldsymbol{z}}} + \boldsymbol{\gamma}^{(n)\mathrm{T}}\frac{\partial\boldsymbol{C}^{(n)}}{\partial\boldsymbol{W}^{(n)}}\frac{d\boldsymbol{W}^{(n)}}{d\boldsymbol{a}^{(n)}}\frac{d\boldsymbol{a}^{(n)}}{d\bar{\boldsymbol{z}}}\right. \\ &\qquad\left. + \boldsymbol{\gamma}^{(n)\mathrm{T}}\frac{\partial\boldsymbol{C}^{(n)}}{\partial\boldsymbol{W}^{(n)}}\frac{d\boldsymbol{W}^{(n)}}{d\bar{\boldsymbol{z}}}\right) \\ &+ \sum_{n=2}^{N}\left(\boldsymbol{\gamma}^{(n)\mathrm{T}}\frac{\partial\boldsymbol{C}^{(n)}}{\partial\boldsymbol{W}^{(n-1)}}\frac{d\boldsymbol{W}^{(n-1)}}{d\boldsymbol{a}^{(n-1)}}\frac{d\boldsymbol{a}^{(n-1)}}{d\bar{\boldsymbol{z}}} + \boldsymbol{\gamma}^{(n)\mathrm{T}}\frac{\partial\boldsymbol{C}^{(n)}}{\partial\boldsymbol{W}^{(n-1)}}\frac{d\boldsymbol{W}^{(n-1)}}{d\bar{\boldsymbol{z}}}\right).\end{aligned} \tag{5.11}$$

To simplify (5.11), first, the total derivatives on $\boldsymbol{a}$ are formulated as $\frac{d(\cdot)}{d\boldsymbol{a}^{(n)}} = \frac{\partial(\cdot)}{\partial\boldsymbol{a}^{(n)}} + \frac{\partial(\cdot)}{\partial\boldsymbol{W}^{(n)}}\frac{\partial\boldsymbol{W}^{(n)}}{\partial\boldsymbol{a}^{(n)}}$. Secondly, all terms including the implicit derivatives on the state vari-

ables, i.e. $\frac{d\boldsymbol{a}^{(n)}}{d\bar{\boldsymbol{z}}}$ and $\frac{d\boldsymbol{W}^{(n)}}{d\bar{\boldsymbol{z}}}$, are gathered so that (5.11) is rewritten as

$$\begin{aligned}\frac{d\tilde{g}}{d\bar{\boldsymbol{z}}} = \frac{\partial g}{\partial \bar{\boldsymbol{z}}} &+ \sum_{n=1}^{N}\left(\boldsymbol{\lambda}^{(n)\mathrm{T}}\frac{\partial \boldsymbol{R}^{(n)}}{\partial \bar{\boldsymbol{z}}} + \boldsymbol{\gamma}^{(n)\mathrm{T}}\frac{\partial \boldsymbol{C}^{(n)}}{\partial \bar{\boldsymbol{z}}}\right) \\ &+ \sum_{n=1}^{N}\left(\boldsymbol{\lambda}^{(n)\mathrm{T}}\frac{d\boldsymbol{R}^{(n)}}{d\boldsymbol{a}^{(n)}} + \boldsymbol{\lambda}^{(n+1)\mathrm{T}}\frac{d\boldsymbol{R}^{(n+1)}}{d\boldsymbol{a}^{(n)}} + \boldsymbol{\gamma}^{(n)\mathrm{T}}\frac{d\boldsymbol{C}^{(n)}}{d\boldsymbol{a}^{(n)}}\right. \\ &\qquad \left. + \boldsymbol{\gamma}^{(n+1)\mathrm{T}}\frac{d\boldsymbol{C}^{(n+1)}}{d\boldsymbol{a}^{(n)}} + \frac{dg}{d\boldsymbol{a}^{(n)}}\right)\frac{d\boldsymbol{a}^{(n)}}{d\bar{\boldsymbol{z}}} \\ &+ \sum_{n=1}^{N}\left(\boldsymbol{\lambda}^{(n)\mathrm{T}}\frac{\partial \boldsymbol{R}^{(n)}}{\partial \boldsymbol{W}^{(n)}} + \boldsymbol{\lambda}^{(n+1)\mathrm{T}}\frac{\partial \boldsymbol{R}^{(n+1)}}{\partial \boldsymbol{W}^{(n)}} + \boldsymbol{\gamma}^{(n)\mathrm{T}}\frac{\partial \boldsymbol{C}^{(n)}}{\partial \boldsymbol{W}^{(n)}}\right. \\ &\qquad \left. + \boldsymbol{\gamma}^{(n+1)\mathrm{T}}\frac{\partial \boldsymbol{C}^{(n+1)}}{\partial \boldsymbol{W}^{(n)}} + \frac{\partial g}{\partial \boldsymbol{W}^{(n)}}\right)\frac{d\boldsymbol{W}^{(n)}}{d\bar{\boldsymbol{z}}},\end{aligned} \tag{5.12}$$

where $\boldsymbol{\lambda}^{(N+1)}$ and $\boldsymbol{\gamma}^{(N+1)}$ are zero since there only are N time steps. The remaining adjoint vectors are chosen so that the implicit derivatives on $\boldsymbol{a}^{(n)}$ and $\boldsymbol{W}^{(n)}$ with respect to $\bar{\boldsymbol{z}}$ are eliminated. It should also be noted that since $\boldsymbol{C}^{(n)} = \boldsymbol{0}$ should be fulfilled for all displacements $\boldsymbol{a}^{(n)}$, it holds that $\frac{d\boldsymbol{C}^{(n)}}{d\boldsymbol{a}^{(n)}} = \boldsymbol{0}$ [1]. It turns out that (5.12) is a terminal value problem that can be solved sequently from $n = N, N-1, ..., 1$ via

$$\begin{aligned}\left(\frac{d\boldsymbol{R}^{(n)}}{d\boldsymbol{a}^{(n)}}\right)^{\mathrm{T}}\boldsymbol{\lambda}^{(n)} &= -\left(\frac{dg}{d\boldsymbol{a}^{(n)}}\right)^{\mathrm{T}} - \boldsymbol{f}_{\lambda}, \\ \left(\frac{\partial \boldsymbol{C}^{(n)}}{\partial \boldsymbol{W}^{(n)}}\right)^{\mathrm{T}}\boldsymbol{\gamma}^{(n)} &= -\left(\frac{\partial g}{\partial \boldsymbol{W}^{(n)}}\right)^{\mathrm{T}} - \left(\frac{\partial \boldsymbol{R}^{(n)}}{\partial \boldsymbol{W}^{(n)}}\right)^{\mathrm{T}}\boldsymbol{\lambda}^{(n)} - \boldsymbol{f}_{\gamma},\end{aligned} \tag{5.13}$$

where the path-dependent contributions $\boldsymbol{f}_{\lambda}$ and $\boldsymbol{f}_{\gamma}$ for completeness are given by

$$\begin{aligned}\boldsymbol{f}_{\lambda}\left(\boldsymbol{\lambda}^{(n+1)}, \boldsymbol{\gamma}^{(n+1)}\right) &= \left(\frac{d\boldsymbol{R}^{(n+1)}}{d\boldsymbol{a}^{(n)}}\right)^{\mathrm{T}}\boldsymbol{\lambda}^{(n+1)} + \left(\frac{d\boldsymbol{C}^{(n+1)}}{d\boldsymbol{a}^{(n)}}\right)^{\mathrm{T}}\boldsymbol{\gamma}^{(n+1)}, \\ \boldsymbol{f}_{\gamma}\left(\boldsymbol{\lambda}^{(n+1)}, \boldsymbol{\gamma}^{(n+1)}\right) &= \left(\frac{\partial \boldsymbol{R}^{(n+1)}}{\partial \boldsymbol{W}^{(n)}}\right)^{\mathrm{T}}\boldsymbol{\lambda}^{(n+1)} + \left(\frac{\partial \boldsymbol{C}^{(n+1)}}{\partial \boldsymbol{W}^{(n)}}\right)^{\mathrm{T}}\boldsymbol{\gamma}^{(n+1)}.\end{aligned} \tag{5.14}$$

Solving the state problem provides $\boldsymbol{a}^{(n)}$ and $\boldsymbol{W}^{(n)}$, which are used to solve the terminal boundary value problem for $\boldsymbol{\lambda}^{(n)}$ and $\boldsymbol{\gamma}^{(n)}$. The system matrices in (5.13) are

[1] This relation is also used when computing the implicit derivative $\frac{d\boldsymbol{W}^{(n)}}{d\boldsymbol{a}^{(n)}}$.

essentially the same as for the primal problem, and thus, the adjoint sensitivity analysis resembles that of the state problem. This procedure is conceptualized in Fig. 5.1.

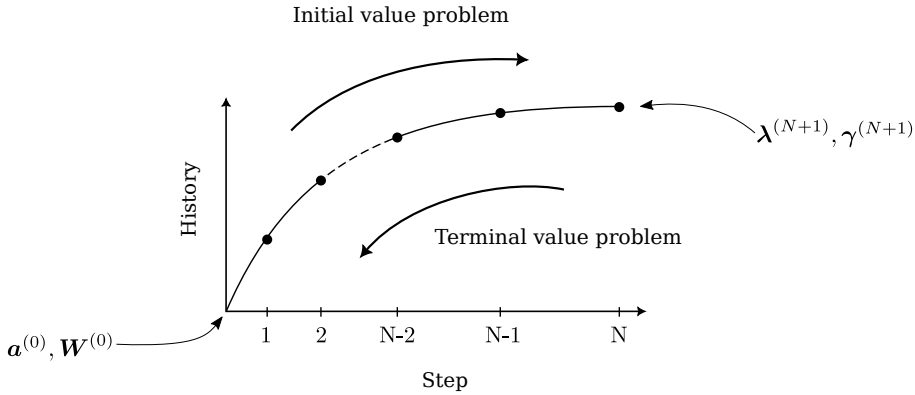

Figure 5.1: Conceptualization of path-dependent initial value problem for the state variables, and the path-dependent terminal value problem for the adjoint vectors.

When the adjoint vectors are found, the sensitivity (5.12) is reduced to

$$\frac{d\tilde{g}}{d\bar{\boldsymbol{z}}} = \frac{\partial g}{\partial \bar{\boldsymbol{z}}} + \sum_{n=1}^{N} \left(\boldsymbol{\lambda}^{(n)\mathrm{T}} \frac{\partial \boldsymbol{R}^{(n)}}{\partial \bar{\boldsymbol{z}}} + \boldsymbol{\gamma}^{(n)\mathrm{T}} \frac{\partial \boldsymbol{C}^{(n)}}{\partial \bar{\boldsymbol{z}}} \right). \tag{5.15}$$

Remark: From a computational point of view, adjoint contributions in the sum in (5.15) can be calculated and assembled once the adjoint vectors for one time step has been determined. This mitigates the need of allocating memory for all adjoint vectors, which can be of significant size if many time steps are considered. However, the state solutions for every time step are required to solve the adjoint vectors, and thus have to be stored. For large-scale problems, one can make use of check-pointing schemes (Kristiansen and Aage (2022)) in order to reduce the memory requirements, where snap shots of the state solution vectors are stored, and then recomputed during the sensitivity analysis. This approach however, comes with an additional computational cost, but reduces the memory requirements.

3.1 Example: Transient thermo-elasticity

Coupled thermo-elasticity is defined by the residual vectors (3.2) and (3.5) such that

$$\boldsymbol{R}^{(n)} = \begin{cases} \boldsymbol{R}_u^{(n)} \left(\bar{\boldsymbol{z}}, \boldsymbol{a}_u^{(n)}, \boldsymbol{a}_\theta^{(n)} \right) = \boldsymbol{0} \\ \boldsymbol{R}_\theta^{(n)} \left(\bar{\boldsymbol{z}}, \boldsymbol{a}_u^{(n)}, \boldsymbol{a}_\theta^{(n)}, \boldsymbol{a}_\theta^{(n-1)} \right) = \boldsymbol{0} \end{cases}, \tag{5.16}$$

should be fulfilled for all time step $n = 1, ..., N$. Since the process is reversible, $\boldsymbol{C}^{(n)}$ in (5.3) and $\boldsymbol{\gamma}^{(n)}$ in (5.8) vanish. Initial values on the nodal temperature vector, $\boldsymbol{a}_\theta^{(0)}$ and the nodal displacement vector $\boldsymbol{a}_u^{(0)}$, are required to solve the initial value problem for all $\boldsymbol{a}_u^{(n)}$ and $\boldsymbol{a}_\theta^{(n)}$.

Assuming three time steps, i.e. $N = 3$, the adjoint vectors are calculated via (5.13) and (5.14) with the terminal values $\boldsymbol{\lambda}^{(4)} = \boldsymbol{0}$. Starting at $N = 3$ provides the stepwise solution procedure

$$\downarrow \begin{cases} \left(\dfrac{d\boldsymbol{R}^{(3)}}{d\boldsymbol{a}^{(3)}}\right)^{\mathrm{T}} \boldsymbol{\lambda}^{(3)} = -\left(\dfrac{dg}{d\boldsymbol{a}^{(3)}}\right)^{\mathrm{T}} \\ \left(\dfrac{d\boldsymbol{R}^{(2)}}{d\boldsymbol{a}^{(2)}}\right)^{\mathrm{T}} \boldsymbol{\lambda}^{(2)} = -\left(\dfrac{dg}{d\boldsymbol{a}^{(2)}}\right)^{\mathrm{T}} - \left(\dfrac{d\boldsymbol{R}^{(3)}}{d\boldsymbol{a}^{(2)}}\right)^{\mathrm{T}} \boldsymbol{\lambda}^{(3)}, \\ \left(\dfrac{d\boldsymbol{R}^{(1)}}{d\boldsymbol{a}^{(1)}}\right)^{\mathrm{T}} \boldsymbol{\lambda}^{(1)} = -\left(\dfrac{dg}{d\boldsymbol{a}^{(1)}}\right)^{\mathrm{T}} - \left(\dfrac{d\boldsymbol{R}^{(2)}}{d\boldsymbol{a}^{(1)}}\right)^{\mathrm{T}} \boldsymbol{\lambda}^{(2)} \end{cases} \tag{5.17}$$

and once all adjoint vectors are found, the total gradients are assemble via (5.15).

For the coupled thermo-mechanical problem, the Jacobian matrix $\left(\frac{d\boldsymbol{R}^{(n)}}{d\boldsymbol{a}^{(n)}}\right)^{\mathrm{T}}$ and the adjoint vectors $\boldsymbol{\lambda}^{(n)}$ are partitioned as

$$\left(\frac{d\boldsymbol{R}^{(n)}}{d\boldsymbol{a}^{(n)}}\right)^{\mathrm{T}} = \begin{bmatrix} \frac{d\boldsymbol{R}_u^{(n)}}{d\boldsymbol{a}_u^{(n)}} & \left(\frac{d\boldsymbol{R}_\theta^{(n)}}{d\boldsymbol{a}_u^{(n)}}\right)^{\mathrm{T}} \\ \left(\frac{d\boldsymbol{R}_u^{(n)}}{d\boldsymbol{a}_\theta^{(n)}}\right)^{\mathrm{T}} & \frac{d\boldsymbol{R}_\theta^{(n)}}{d\boldsymbol{a}_\theta^{(n)}} \end{bmatrix}, \quad \boldsymbol{\lambda}^{(n)} = \begin{bmatrix} \boldsymbol{\lambda}_u^{(n)} \\ \boldsymbol{\lambda}_\theta^{(n)} \end{bmatrix}, \tag{5.18}$$

which itself is a coupled adjoint problem.

3.2 Example: Elasto-plasticity

For the elasto-plastic case, the nested residual formulation is

$$\begin{cases} \boldsymbol{R}^{(n)} = \boldsymbol{R}_u^{(n)}\left(\bar{\boldsymbol{z}}, \boldsymbol{a}_u^{(n)}, \boldsymbol{W}^{(n)}\right) = \boldsymbol{0} \\ \boldsymbol{C}^{(n)} = \boldsymbol{C}^{(n)}\left(\bar{\boldsymbol{z}}, \boldsymbol{a}_u^{(n)}, \boldsymbol{W}^{(n)}, \boldsymbol{W}^{(n-1)}\right) = \boldsymbol{0} \end{cases}. \tag{5.19}$$

To avoid keeping track of the elasto-plastic switches during the adjoint computations, the consistency condition $f\left(\boldsymbol{\xi}^{(n)}, R^{(n)}\right) = 0$ in (3.11) can be replaced by the KKT-condition $\Delta\gamma^{(n)} g = 0$, expressed in the reduced consistency condition (3.16), since it

is fulfilled for both elastic $\left(\Delta\gamma^{(n)}=0\right)$ and plastic $(g=0)$ response. These modifications results in the local plastic equations

$$\boldsymbol{c}^{(n)}\left(\boldsymbol{\epsilon}^{(n)},\boldsymbol{w}^{(n)},\boldsymbol{w}^{(n-1)}\right)=\begin{cases}\boldsymbol{\epsilon}^{pl\,(n)}-\boldsymbol{\epsilon}^{pl\,(n-1)}-\Delta\gamma^{(n)}\boldsymbol{n}^{(n)}=\boldsymbol{0}\\ \boldsymbol{\beta}^{(n)}-\boldsymbol{\beta}^{(n-1)}-\frac{2}{3}H\Delta\gamma^{(n)}\boldsymbol{n}^{(n)}=\boldsymbol{0}\\ \Delta\gamma^{(n)}g\left(\boldsymbol{\epsilon}^{(n)},\boldsymbol{\epsilon}^{pl\,(n-1)},\boldsymbol{\beta}^{(n-1)},\alpha^{(n)},\alpha^{(n-1)}\right)=0\end{cases}, \tag{5.20}$$

which is assembled into the global quantity $\boldsymbol{C}^{(n)}$. Similarly, $\boldsymbol{W}^{(n)}$ represents the assembly of all local plastic state variables in $\boldsymbol{w}^{(n)}=\left\{\boldsymbol{\epsilon}^{pl\,(n)},\boldsymbol{\beta}^{(n)},\alpha^{(n)}\right\}$. Note that $\Delta\gamma^{(n)}$ in (5.20) should be seen as a variables explicitly determined by $\alpha^{(n)}$ and $\alpha^{(n-1)}$.

Once again, assuming three time steps, and the terminal values $\boldsymbol{\lambda}^{(4)}=\boldsymbol{0}$ and $\boldsymbol{\gamma}^{(4)}=\boldsymbol{0}$ provides the stepwise solution procedure

$$\downarrow\begin{cases}\begin{cases}\left(\frac{d\boldsymbol{R}^{(3)}}{d\boldsymbol{a}^{(3)}}\right)^{\mathrm{T}}\boldsymbol{\lambda}^{(3)}=-\left(\frac{dg}{d\boldsymbol{a}^{(3)}}\right)^{\mathrm{T}}\\ \left(\frac{\partial\boldsymbol{C}^{(3)}}{\partial\boldsymbol{W}^{(3)}}\right)^{\mathrm{T}}\boldsymbol{\gamma}^{(3)}=-\left(\frac{\partial g}{\partial\boldsymbol{W}^{(3)}}\right)^{\mathrm{T}}-\left(\frac{\partial\boldsymbol{R}^{(3)}}{\partial\boldsymbol{W}^{(3)}}\right)^{\mathrm{T}}\boldsymbol{\lambda}^{(3)}\end{cases}\\ \begin{cases}\left(\frac{d\boldsymbol{R}^{(2)}}{d\boldsymbol{a}^{(2)}}\right)^{\mathrm{T}}\boldsymbol{\lambda}^{(2)}=-\left(\frac{dg}{d\boldsymbol{a}^{(2)}}\right)^{\mathrm{T}}-\left(\frac{d\boldsymbol{R}^{(3)}}{d\boldsymbol{a}^{(2)}}\right)^{\mathrm{T}}\boldsymbol{\lambda}^{(3)}-\left(\frac{d\boldsymbol{C}^{(3)}}{d\boldsymbol{a}^{(2)}}\right)^{\mathrm{T}}\boldsymbol{\gamma}^{(3)}\\ \left(\frac{\partial\boldsymbol{C}^{(2)}}{\partial\boldsymbol{W}^{(2)}}\right)^{\mathrm{T}}\boldsymbol{\gamma}^{(2)}=-\left(\frac{\partial g}{\partial\boldsymbol{W}^{(2)}}\right)^{\mathrm{T}}-\left(\frac{\partial\boldsymbol{R}^{(2)}}{\partial\boldsymbol{W}^{(2)}}\right)^{\mathrm{T}}\boldsymbol{\lambda}^{(2)}-\left(\frac{\partial\boldsymbol{C}^{(3)}}{\partial\boldsymbol{W}^{(2)}}\right)^{\mathrm{T}}\boldsymbol{\gamma}^{(3)}\end{cases}\\ \begin{cases}\left(\frac{d\boldsymbol{R}^{(1)}}{d\boldsymbol{a}^{(1)}}\right)^{\mathrm{T}}\boldsymbol{\lambda}^{(1)}=-\left(\frac{dg}{d\boldsymbol{a}^{(1)}}\right)^{\mathrm{T}}-\left(\frac{d\boldsymbol{R}^{(2)}}{d\boldsymbol{a}^{(1)}}\right)^{\mathrm{T}}\boldsymbol{\lambda}^{(2)}-\left(\frac{d\boldsymbol{C}^{(2)}}{d\boldsymbol{a}^{(1)}}\right)^{\mathrm{T}}\boldsymbol{\gamma}^{(2)}\\ \left(\frac{\partial\boldsymbol{C}^{(1)}}{\partial\boldsymbol{W}^{(1)}}\right)^{\mathrm{T}}\boldsymbol{\gamma}^{(1)}=-\left(\frac{\partial g}{\partial\boldsymbol{W}^{(1)}}\right)^{\mathrm{T}}-\left(\frac{\partial\boldsymbol{R}^{(1)}}{\partial\boldsymbol{W}^{(1)}}\right)^{\mathrm{T}}\boldsymbol{\lambda}^{(1)}-\left(\frac{\partial\boldsymbol{C}^{(2)}}{\partial\boldsymbol{W}^{(1)}}\right)^{\mathrm{T}}\boldsymbol{\gamma}^{(2)}\end{cases}\end{cases}. \tag{5.21}$$

In the procedure above, $\boldsymbol{\lambda}$ is first solved for and then used to compute $\boldsymbol{\gamma}$. This procedure resembles that of the primal state update in the sense that $\boldsymbol{\lambda}$ and $\boldsymbol{\gamma}$ are related to the enforced residual equations, and therefore analogous to the displacement vector and the plastic state variables, respectively. It is possible to reduce the linear system for $\boldsymbol{\gamma}$ further so that an update scheme of local adjoint variables is obtained. This reduction provides an adjoint solution procedure that is consistent with the primal solution procedure, and is presented in detail in Paper C.

Once the adjoint vectors have been obtained, the final expression for the gradients are assembled via (5.15).

Chapter 6

Future work

During the development of research methods, assumptions and simplifications are always introduced. The presented methods and frameworks can be extended to improve efficiency and broaden the range of applications. Some ideas and perspectives regarding this topic is presented herein.

1 Dominating boundary effects

In the finite element simulations, stress concentrations may arise at boundaries with fixed displacements since the rigid boundary conditions prevents any deformation at the constrained points. This leads to artificially large stress values that remains throughout the optimization since the stiffness is infinite at these points, potentially leading to large stress gradients. In stress-based topology optimization, these singularities may lead to conservative designs where the optimization is driven by the stress at these boundaries.

This effect can be a challenge especially for stress constrained, or plasticity-based problems since local stress values drives the optimization. To improve numerical stability, these regions can be ignored in the optimization problem, or areas near the fixed supports can be prescribed with material and excluded from the design domain. However, other more sophisticated approaches may improve the optimized results.

A remedy to this issue could be to increase the mesh resolution near fixed boundaries where e.g. adaptive mesh refinement based on high stress regions or stress error estimation could be included. This could better capture the sharp stress gradient from the boundary, which in turn could improve both the numerical stability of the optimization and the stress calculations in the simulation.

2 Time integration errors

For path-dependent problems, numerical time integration is required. In topology optimization problems, it is common to consider first order implicit methods, and base the time increment sizes on empirical testing. However, since the design is drastically changed, this may lead to inconsistent time integration errors between designs.

One suggestion to improve accuracy, and keep a consistent integration errors, would be to introduce a higher order time integration scheme with adaptive time increments based on an error estimation. For instance, Diagonally Implicit Runge-Kutta integration methods where an error estimation can be used to find an adaptive time step.

3 Improved boundary representations

Due to the density-based optimization approach, the design lacks of exact boundary representation since the boundary of the design is represented by a steep gradient in the design field rather than fixed geometrical points. To resolve the boundary, increased mesh resolution is required, which leads to computationally heavy problems.

The advantage of shape optimization compared to topology optimization is that the boundary representation is significantly improved. The combination of these two methods could be used to deliver a more reliable solution where the topology optimization provides a general idea of the design, and the shape optimization works as fine tuning. A simultaneous approach could also be employed as done by Dalklint et al. (2024) and Dahlberg et al. (2025).

4 Adaptive mesh refinement and unstructured grids

Adaptive mesh refinement can be used not only to improve the accuracy in the finite element simulations, but also to redistribute the elements in the mesh so that not an unnecessary amount of element is considered in void regions. Since only structured grids has been considered in this thesis, the void regions are modeled with a large amount of elements, which contributes to the computational cost.

For large-scale problems, adaptive mesh refinement and unstructured grids could improve the computational efficiency. This of course introduces a challenge from a parallelization point of view on how the mesh regions should be distributed over the ranks for well balanced work load.

Chapter 7

Summary of the appended papers

Paper A: A framework for stress-constrained topology optimization of hyperelastic structures subjected to non-proportional loading is established. Due to the non-proportional loading history, the stress must be constrained at every spatial and temporal point throughout the load trajectory, potentially resulting in an excessive number of stress constraints. To efficiently handle this, the augmented Lagrangian method is employed, replacing the original constrained optimization problem with a single Lagrangian function. Numerical examples examine the impact of different load trajectories leading to the same terminal load, demonstrating that considering the entire load trajectory significantly influences the optimized designs.

Paper B: Multi-material topology optimization is applied to the design of thermal actuators operating under transient thermal conditions. The materials are modeled using a finite strain thermo-hyperelastic formulation, combined with an energy interpolation scheme developed for thermo-elasticity. The actuators are designed for optimal performance within a limited time, and numerical examples demonstrate that the material distribution is significantly influenced by the duration of heat application.

Paper C: A large-scale framework for elasto-plastic topology optimization is established under the smal strain assumption. The coaxiality between the plastic strain rate and the stress is exploited to formulate a consistent and efficient adjoint sensitivity analysis scheme. The implementation is carried out using the scientific computing library PETSc, enabling the design of structures discretized with multiple million finite elements. Numerical examples demonstrate the functionality and potential of the developed framework by designing energy absorbing structures and structures with tailored mechanical responses with high mesh resolution.

Paper D: A novel objective for elasto-plastic topology optimization is investigated in the design of permanent lock mechanisms. Kinematic hardening is considered to accurately capture the Bauschinger effect, where structures undergo a single load cycle to maximize the output displacement and retain a desired deformed shape after unloading. This methodology introduces a new class of design problems that explicitly consider the unloaded state. The approach is demonstrated through numerical examples, including the design of a permanently deformed lock mechanism and a complex compression-torsion conversion device.

Paper E: The stiffness definition of elasto-plastic structures is investigated by comparing the traditional end-compliance formulation with a novel end-tangent stiffness formulation. The proposed formulation allows structures to be optimized for maximum end-tangent stiffness, in contrast to end compliance, which corresponds to secant stiffness. Numerical examples demonstrate that the two formulations yield distinctly different designs with significantly different structural responses. Structures optimized for end-tangent stiffness exhibit end tangent stiffness magnitudes far greater than those optimized for end compliance, which are near collapse at the terminal load step.

Bibliography

Aage, N., Andreassen, E., Lazarov, B.S., 2015. Topology optimization using petsc: An easy-to-use, fully parallel, open source topology optimization framework. Structural and Multidisciplinary Optimization 51, 565–572.

Aage, N., Andreassen, E., Lazarov, B.S., Sigmund, O., 2017. Giga-voxel computational morphogenesis for structural design. Nature 550, 84–86.

Abueidda, D.W., Kang, Z., Koric, S., James, K.A., Jasiuk, I.M., 2021. Topology optimization for three-dimensional elastoplastic architected materials using a path-dependent adjoint method. International Journal for Numerical Methods in Engineering 122, 1889–1910.

Allaire, G., Jouve, F., Toader, A.M., 2004. Structural optimization using sensitivity analysis and a level-set method. Journal of computational physics 194, 363–393.

Amir, O., 2017. Stress-constrained continuum topology optimization: a new approach based on elasto-plasticity. Structural and Multidisciplinary Optimization 55, 1797–1818.

Amir, O., Stolpe, M., Sigmund, O., 2010. Efficient use of iterative solvers in nested topology optimization. Structural and Multidisciplinary Optimization 42, 55–72.

Bathe, K.J., 2006. Finite element procedures. Klaus-Jurgen Bathe.

Bendsøe, M.P., 1989. Optimal shape design as a material distribution problem. Structural optimization 1, 193–202. doi:10.1007/BF01650949.

Bendsøe, M.P., Kikuchi, N., 1988. Generating optimal topologies in structural design using a homogenization method. Computer methods in applied mechanics and engineering 71, 197–224.

Blank, L., Garcke, H., Sarbu, L., Srisupattarawanit, T., Styles, V., Voigt, A., 2012. Phase-field approaches to structural topology optimization. Constrained optimization and optimal control for partial differential equations , 245–256.

Borrvall, T., Petersson, J., 2001a. Large-scale topology optimization in 3d using parallel computing. Computer methods in applied mechanics and engineering 190, 6201–6229.

Borrvall, T., Petersson, J., 2001b. Topology optimization using regularized intermediate density control. Computer Methods in Applied Mechanics and Engineering 190, 4911–4928.

Bourdin, B., 2001. Filters in topology optimization. International journal for numerical methods in engineering 50, 2143–2158.

Bourdin, B., Chambolle, A., 2003. Design-dependent loads in topology optimization. ESAIM: Control, Optimisation and Calculus of Variations 9, 19–48.

Bruggi, M., 2008. On an alternative approach to stress constraints relaxation in topology optimization. Structural and multidisciplinary optimization 36, 125–141. doi:10.1007/s00158-007-0203-6.

Bruns, T.E., Tortorelli, D.A., 2001. Topology optimization of non-linear elastic structures and compliant mechanisms. Computer methods in applied mechanics and engineering 190, 3443–3459.

Cheng, G.D., Guo, X., 1997. ε-relaxed approach in structural topology optimization. Structural optimization 13, 258–266.

Dahlberg, V., Dalklint, A., Wallin, M., 2025. Simultaneous shape and topology optimization on unstructured grids. Computer Methods in Applied Mechanics and Engineering 438, 117830.

Dalklint, A., Wallin, M., Tortorelli, D., 2024. Simultaneous shape and topology optimization of inflatable soft robots. Computer Methods in Applied Mechanics and Engineering 420, 116751.

Dalklint, A., Wallin, M., Tortorelli, D.A., 2020. Eigenfrequency constrained topology optimization of finite strain hyperelastic structures. Structural and Multidisciplinary Optimization 61, 2577–2594.

Dbouk, T., 2017. A review about the engineering design of optimal heat transfer systems using topology optimization. Applied Thermal Engineering 112, 841–854.

De Borst, R., Crisfield, M.A., Remmers, J.J., Verhoosel, C.V., 2012. Nonlinear finite element analysis of solids and structures. John Wiley & Sons.

Duysinx, P., Bendsøe, M.P., 1998. Topology optimization of continuum structures with local stress constraints. International journal for numerical methods in engineering 43, 1453–1478.

Ferrari, F., Sigmund, O., 2019. Revisiting topology optimization with buckling constraints. Structural and Multidisciplinary Optimization 59, 1401–1415.

Gao, T., Zhang, W., Zhu, J., Xu, Y., Bassir, D.H., 2008. Topology optimization of heat conduction problem involving design-dependent heat load effect. Finite Elements in Analysis and Design 44, 805–813.

Gao, X., Ma, H., 2015. Topology optimization of continuum structures under buckling constraints. Computers & Structures 157, 142–152.

Gersborg-Hansen, A., Bendsøe, M.P., Sigmund, O., 2006. Topology optimization of heat conduction problems using the finite volume method. Structural and multidisciplinary optimization 31, 251–259.

Giraldo-Londoño, O., Mirabella, L., Dalloro, L., Paulino, G.H., 2020. Multi-material thermomechanical topology optimization with applications to additive manufacturing: Design of main composite part and its support structure. Computer Methods in Applied Mechanics and Engineering 363, 112812.

Granlund, G., Wallin, M., 2024. Large-scale elasto-plastic topology optimization. International Journal for Numerical Methods in Engineering , e7583.

Granlund, G., Wallin, M., 2025. Designing compliant self-locking structures using topology optimization. Accepted for publication in Structural and Multidisciplinary Optimization .

Granlund, G., Wallin, M., Günther-Hanssen, O., Tortorelli, D., Watts, S., 2024. Topology optimization of compliant mechanisms under transient thermal conditions. Computer Methods in Applied Mechanics and Engineering 418, 116478.

Hård, D., Wallin, M., Ristinmaa, M., 2024. Connectivity constraints ensuring continuous electrodes in topology optimization of electroactive polymer. Journal of Mechanical Design 146.

Holzapfel, G., 2000. Nonlinear Solid Mechanics: A Continuum Approach for Engineering. Wiley.

Hvejsel, C., Lund, E., 2011. Material interpolation schemes for unified topology and multi-material optimization. Struct Multidisc Optim 43, 811–825. doi:10.1007/s00158-011-0625-z.

Ivarsson, N., Wallin, M., Amir, O., Tortorelli, D.A., 2021. Plastic work constrained elastoplastic topology optimization. International Journal for Numerical Methods in Engineering 122, 4354–4377.

Ivarsson, N., Wallin, M., Tortorelli, D., 2018. Topology optimization of finite strain viscoplastic systems under transient loads. International Journal for Numerical Methods in Engineering 114, 1351–1367.

Jensen, J.S., Nakshatrala, P.B., Tortorelli, D.A., 2014. On the consistency of adjoint sensitivity analysis for structural optimization of linear dynamic problems. Structural and Multidisciplinary Optimization 49, 831–837.

Kato, J., Hoshiba, H., Takase, S., Terada, K., Kyoya, T., 2015. Analytical sensitivity in topology optimization for elastoplastic composites. Structural and Multidisciplinary Optimization 52, 507–526.

Kemmler, R., Lipka, A., Ramm, E., 2005. Large deformations and stability in topology optimization. Structural and Multidisciplinary Optimization 30, 459–476.

Kristiansen, H., Aage, N., 2022. An open-source framework for large-scale transient topology optimization using petsc. Structural and Multidisciplinary Optimization 65, 295.

Lazarov, B.S., Sigmund, O., 2011. Filters in topology optimization based on helmholtz-type differential equations. International Journal for Numerical Methods in Engineering 86, 765–781. doi:10.1002/nme.3072.

Le, C., Norato, J., Bruns, T., Ha, C., Tortorelli, D., 2010. Stress-based topology optimization for continua. Structural and Multidisciplinary Optimization 41, 605–620.

Li, L., Khandelwal, K., 2015. Volume preserving projection filters and continuation methods in topology optimization. Engineering Structures 85, 144–161.

Li, Y., Saitou, K., Kikuchi, N., 2004. Topology optimization of thermally actuated compliant mechanisms considering time-transient effect. Finite elements in analysis and design 40, 1317–1331.

Maute, K., Schwarz, S., Ramm, E., 1998. Adaptive topology optimization of elastoplastic structures. Structural optimization 15, 81–91.

Michaleris, P., Tortorelli, D.A., Vidal, C.A., 1994. Tangent operators and design sensitivity formulations for transient non-linear coupled problems with applications to elastoplasticity. International Journal for Numerical Methods in Engineering 37, 2471–2499.

Neves, M., Rodrigues, H., Guedes, J., 1995. Generalized topology design of structures with a buckling load criterion. Structural optimization 10, 71–78.

Osher, S., Fedkiw, R.P., 2001. Level set methods: an overview and some recent results. Journal of Computational physics 169, 463–502.

Ottosen, N.S., Ristinmaa, M., 2005. The mechanics of constitutive modeling. Elsevier.

Pedersen, C.B., 2002. Revisiting topology optimization of continuum structures with elastoplastic response. j for 1, 2.

Pedersen, C.B., 2003. Topology optimization design of crushed 2d-frames for desired energy absorption history. Structural and Multidisciplinary Optimization 25, 368–382.

Pedersen, N.L., 2000. Maximization of eigenvalues using topology optimization. Structural and multidisciplinary optimization 20, 2–11.

Russ, J.B., Waisman, H., 2021. A novel elastoplastic topology optimization formulation for enhanced failure resistance via local ductile failure constraints and linear buckling analysis. Computer Methods in Applied Mechanics and Engineering 373, 113478.

Sethian, J.A., 2001. Evolution, implementation, and application of level set and fast marching methods for advancing fronts. Journal of computational physics 169, 503–555.

Sigmund, O., 1997. On the design of compliant mechanisms using topology optimization. Journal of Structural Mechanics 25, 493–524.

Sigmund, O., 2001a. Design of multiphysics actuators using topology optimization–part i: One-material structures. Computer methods in applied mechanics and engineering 190, 6577–6604.

Sigmund, O., 2001b. Design of multiphysics actuators using topology optimization–part ii: Two-material structures. Computer methods in applied mechanics and engineering 190, 6605–6627.

Sigmund, O., Maute, K., 2013. Topology optimization approaches: A comparative review. Structural and multidisciplinary optimization 48, 1031–1055.

da Silva, G.A., Aage, N., Beck, A.T., Sigmund, O., 2021. Three-dimensional manufacturing tolerant topology optimization with hundreds of millions of local stress constraints. International Journal for Numerical Methods in Engineering 122, 548–578.

Simo, J., Hughes, T., 2006. Computational inelasticity. volume 7. Springer Science & Business Media.

Stolpe, M., Svanberg, K., 2001. An alternative interpolation scheme for minimum compliance topology optimization. Structural and Multidisciplinary Optimization 22, 116–124. doi:10.1007/s001580100129.

Thillaithevan, D., Murphy, R., Hewson, R., Santer, M., 2024. Inverse design of periodic microstructures with targeted nonlinear mechanical behaviour. Structural and Multidisciplinary Optimization 67, 1615–1488.

Träff, E.A., Rydahl, A., Karlsson, S., Sigmund, O., Aage, N., 2023. Simple and efficient gpu accelerated topology optimisation: Codes and applications. Computer Methods in Applied Mechanics and Engineering 410, 116043.

Van Dijk, N.P., Maute, K., Langelaar, M., Van Keulen, F., 2013. Level-set methods for structural topology optimization: a review. Structural and Multidisciplinary Optimization 48, 437–472.

Verbart, A., Langelaar, M., Keulen, F.v., 2017. A unified aggregation and relaxation approach for stress-constrained topology optimization. Structural and Multidisciplinary Optimization 55, 663–679.

Wallin, M., Ivarsson, N., Tortorelli, D., 2018. Stiffness optimization of non-linear elastic structures. Computer Methods in Applied Mechanics and Engineering 330, 292–307.

Wallin, M., Jönsson, V., Wingren, E., 2016. Topology optimization based on finite strain plasticity. Structural and multidisciplinary optimization 54, 783–793.

Wallin, M., Ristinmaa, M., Askfelt, H., 2012. Optimal topologies derived from a phase-field method. Structural and Multidisciplinary Optimization 45, 171–183.

Wang, F., Lazarov, B., Sigmund, O., 2014. Interpolation scheme for fictitious domain techniques and topology optimization of finite strain elastic problems. Computer Methods in Applied Mechanics and Engineering 276, 453–472. doi:10.1016/j.cma.2014.03.021.

Wang, F., Lazarov, B.S., Sigmund, O., 2011. On projection methods, convergence and robust formulations in topology optimization. Structural and multidisciplinary optimization 43, 767–784.

Wu, S., Zhang, Y., Liu, S., 2019. Topology optimization for minimizing the maximum temperature of transient heat conduction structure. Structural and Multidisciplinary Optimization 60, 69–82.

Zhang, G., Alberdi, R., Khandelwal, K., 2018. Topology optimization with incompressible materials under small and finite deformations using mixed u/p elements. International Journal for Numerical Methods in Engineering 115, 1015–1052.

Zienkiewicz, O.C., Taylor, R.L., 2000. The finite element method: solid mechanics. volume 2. Butterworth-heinemann.